



Cite this: *Nanoscale Adv.*, 2025, 7, 6032

## Fabrication of $\text{TiO}_2@\text{SnS}_2$ core–shell nanocomposites *via* a thermal decomposition approach for sunlight-driven photodegradation of crystal violet

Nainy Khera and Jeevanandam Pethaiyan \*

In the current study,  $\text{TiO}_2@\text{SnS}_2$  core–shell nanocomposites were prepared *via* a facile thermal decomposition method. The synthesis consists of thermal decomposition of tin chloride pentahydrate and thiourea in the presence of NaOH-modified  $\text{TiO}_2$  microspheres in diphenyl ether (DPE) at  $\sim 200$  °C in air. The synthesized  $\text{TiO}_2@\text{SnS}_2$  core–shell nanocomposites were characterized by XRD, FT-IR, TGA, FESEM, TEM, EDXA, UV-DRS, PL and XPS. The XRD results indicate the presence of both  $\text{TiO}_2$  and  $\text{SnS}_2$  phases in the core–shell nanocomposites. FESEM, TEM and EDX analyses results confirm uniform coating of  $\text{SnS}_2$  nanoparticles on the surface modified  $\text{TiO}_2$  microspheres. XPS analysis results confirm the presence of  $\text{Sn}^{4+}$ ,  $\text{Ti}^{4+}$ ,  $\text{O}^{2-}$  and  $\text{S}^{2-}$  in the  $\text{TiO}_2@\text{SnS}_2$  nanocomposites. After their characterization, the  $\text{TiO}_2@\text{SnS}_2$  core–shell nanocomposites were explored for their catalytic activity towards the photodegradation of a toxic dye (crystal violet (CV)) in an aqueous solution under sunlight. The photodegradation efficiency of  $\text{TiO}_2@\text{SnS}_2$  core–shell nanocomposites is better than that of  $\text{TiO}_2$  microspheres,  $\text{SnS}_2$  nanoparticles and other metal sulfide nanoparticles/nanocomposites reported in the literature.

Received 31st May 2025

Accepted 1st August 2025

DOI: 10.1039/d5na00533g

[rsc.li/nanoscale-advances](http://rsc.li/nanoscale-advances)

## 1 Introduction

Water pollution from dyes threatens ecosystems across the globe. As human population and economies expand, water pollution has become one of the major issues. The unavailability of sufficient freshwater not only affects human life but it also affects biodiversity and other ecosystems.<sup>1</sup> Textile industries produce organic contaminants such as synthetic dyes in high amounts. The dyes do not bind tightly to the fabric and about 20% of them are discharged without any prior treatment into water systems and cause pollution.<sup>2</sup> The toxic dyes are often stable, carcinogenic and poisonous.<sup>3</sup> In the past few decades, scientists have been working on different methods for the treatment of contaminated water. Photocatalysis is widely explored for the degradation of toxic dyes. It has advantages such as use of sunlight, low cost and being an environment friendly process.<sup>4</sup>

Photocatalysts based on metal oxide nanoparticles such as  $\text{TiO}_2$ ,<sup>5</sup>  $\text{MoO}_{3-x}$ ,<sup>6</sup>  $\text{Cu}_2\text{O}$ ,<sup>7</sup>  $\text{WO}_3$ ,<sup>8</sup> and  $\text{NiCo}_2\text{O}_4$ ,<sup>9</sup> and metal sulfide nanoparticles such as  $\text{NiS}$ ,<sup>10</sup>  $\text{MoS}_2$ ,<sup>11</sup>  $\text{CuS}$ ,<sup>12</sup> and  $\text{SnS}_2$ <sup>13</sup> have been explored as catalysts for the degradation of toxic dyes. Several core–shell nanocomposites such as  $\text{CuS}/\text{ZnO}$ ,<sup>14</sup>  $\text{ZnO}/\text{ZnS}$ ,<sup>15</sup>  $\text{CoFe}_2\text{O}_4@\text{CoWO}_4$ ,<sup>16</sup>  $\text{MoO}_3@\text{MoS}_2$ ,<sup>17</sup>  $\text{CdS}/\text{ZnO}$ ,<sup>18</sup>

$\text{TiO}_2@\text{CoFe}_3\text{O}_4$ ,<sup>19</sup>  $\text{WO}_3@\text{TiO}_2$ ,<sup>20</sup>  $\text{ZnIn}_2\text{S}_4@\text{CeO}_2$ ,<sup>21</sup>  $\text{ZnO}@\text{SnS}_2$ ,<sup>22</sup> and  $\alpha\text{-Fe}_2\text{O}_3@\text{SnO}_2/\text{Ti}_3\text{C}_2$ <sup>23</sup> have been explored for the photodegradation of dyes such as methylene blue, congo red, rhodamine B, methyl orange, malachite green, *etc.* and they show better activity than pure metal sulfide and metal oxide nanoparticles.

Different  $\text{SnS}_2$  based nanocomposites are reported in the literature such as  $\text{SnS}_2/\text{chitosan}$ , synthesized *via* the precipitation method, for photodegradation of crystal violet,<sup>24</sup>  $\text{SnS}_2/\text{bi-ochar}$  nanocomposite, synthesized *via* the hydrothermal route, for photodegradation of amoxycillin and congo red,<sup>25</sup>  $\text{SnS}_2/\text{BiVO}_4$  nanocomposite, synthesized *via* the hydrothermal route, for photocatalytic degradation of ciprofloxacin,<sup>26</sup>  $\text{SnS}_2/\text{CdO}$  nanocomposite, synthesized *via* the precipitation method, for photodegradation of RhB and congo red,<sup>27</sup>  $\text{SnS}_2/\text{Ag}_3\text{VO}_4$  nanocomposite, synthesized *via* the hydrothermal method, for photodegradation of methylene blue,<sup>28</sup>  $\text{SnS}_2/\text{NiCo-LDH}$  nanocomposite, synthesized *via* the co-precipitation method, for photodegradation of thiamethoxam,<sup>29</sup> polyaniline/ $\text{SnS}_2$  nanocomposite, synthesized by the hydrothermal method, for hydrogen evolution,<sup>30</sup>  $\text{PVDF}/\text{SnS}_2$  nanocomposite, synthesized *via* the hydrothermal method, for piezoelectric energy harvesting,<sup>31</sup>  $\text{CeO}_2/\text{SnS}_2/\text{polyaniline}$  nanocomposite, synthesized *via* the hydrothermal method, for photocatalytic reduction of  $\text{Cr}(\text{vi})$ ,<sup>32</sup>  $\text{PbS}:\text{SnS}_2$  nanocomposite, synthesized *via* the precipitation method, for ethanol sensing,<sup>33</sup>  $\text{Pd}/\text{SnS}_2/\text{SnO}_2$

Department of Chemistry, Indian Institute of Technology Roorkee, Roorkee-247667, India. E-mail: [jeevafcy@iitr.ac.in](mailto:jeevafcy@iitr.ac.in); Fax: +91-1332-273560; Tel: +91-1332-285444



nanocomposite, synthesized *via* the hydrothermal method, for detection of H<sub>2</sub>,<sup>34</sup> Au/SnS<sub>2</sub> nanocomposite, synthesized *via* chemical reduction method, as a NO<sub>2</sub> gas sensor,<sup>35</sup> MoS<sub>2</sub>/SnS<sub>2</sub> nanocomposite, synthesized *via* the hydrothermal method, as an anode in sodium ion batteries,<sup>36</sup> SnS<sub>2</sub>/CuO nanocomposite, synthesized by the precipitation method, in broadband photodetectors,<sup>37</sup> BiOI@SnS<sub>2</sub> core–shell nanocomposite, synthesized *via* the co-precipitation method, for photodegradation of RhB,<sup>38</sup> and MnFe<sub>2</sub>O<sub>4</sub>@SnS<sub>2</sub> core–shell nanocomposite, synthesized *via* the hydrothermal method, for photodegradation of methylene blue.<sup>39</sup>

TiO<sub>2</sub> is a semiconductor with a wide band gap ( $E_g$  (bulk) = 3.2 eV).<sup>40</sup> It is a well-known semiconductor for environmental remediation and it exhibits high recombination of photogenerated electrons and holes leading to its low photocatalytic activity. SnS<sub>2</sub> is economical and non-toxic with good thermal stability.<sup>41,42</sup> It has a narrow band gap of about 1.9 eV<sup>43</sup> and is known to exhibit good photocatalytic activity.<sup>42,44</sup> To improve the photocatalytic activity of TiO<sub>2</sub> further, formation of a nanocomposite of TiO<sub>2</sub> with SnS<sub>2</sub> has been proposed. Both the valence band (VB) and conduction band (CB) of SnS<sub>2</sub> lie below those of TiO<sub>2</sub>. Due to this, during light irradiation, the photogenerated electrons from the CB of SnS<sub>2</sub> are easily transferred to that of TiO<sub>2</sub>. This enhances the separation of electrons and holes and improves the photocatalytic efficiency.<sup>45</sup> TiO<sub>2</sub>–SnS<sub>2</sub> nanocomposites are useful for various applications such as photodegradation of dyes such as methyl orange, methylene blue and RhB,<sup>46–48</sup> photodegradation of antibiotics such as tetracycline,<sup>49</sup> NO<sub>2</sub> gas sensors,<sup>50,51</sup> humidity sensors,<sup>52,53</sup> protection of stainless steel,<sup>54</sup> photodetectors,<sup>55</sup> H<sub>2</sub> gas production,<sup>56,57</sup> biosensors,<sup>58</sup> photoreduction of Cr(vi),<sup>45</sup> photocatalytic H<sub>2</sub> evolution,<sup>59</sup> anode material in lithium-ion batteries,<sup>60</sup> photodegradation of diclofenac,<sup>61</sup> self-decontaminating textiles,<sup>62</sup> photoelectrochemical water splitting,<sup>63</sup> photodegradation of diethyl sulfide,<sup>64</sup> electrocatalytic oxygen evolution,<sup>65</sup> and photocatalytic reduction of CO<sub>2</sub>.<sup>66</sup>

In the current study, TiO<sub>2</sub>@SnS<sub>2</sub> core–shell nanocomposites have been synthesized. The novelty of this work is as follows. In the literature, TiO<sub>2</sub>–SnS<sub>2</sub> nanocomposites have been reported (e.g., yolk–shell SnS<sub>2</sub>–TiO<sub>2</sub> microsphere composite<sup>67</sup> and SnS<sub>2</sub>@TiO<sub>2</sub> double shell nanocomposite<sup>47</sup>) but the core–shell structure of the nanocomposite (TiO<sub>2</sub>@SnS<sub>2</sub>) has not been previously reported. The thermal decomposition method has been used for the synthesis of different metal sulfide nanoparticles and their nanocomposites. However, the synthesis of a TiO<sub>2</sub>@SnS<sub>2</sub> nanocomposite has not been previously reported using this approach. The reported methods used for the synthesis of TiO<sub>2</sub>–SnS<sub>2</sub> nanocomposites in the literature (solvothermal,<sup>50</sup> hydrothermal,<sup>52</sup> chemical bath deposition,<sup>55</sup> and sol–gel method<sup>61</sup>) have disadvantages such as use of high pressure (50 bar to 2 kbar) and prolonged reaction time (12 h to 16 h). For example, the sol–gel method requires a reaction time of up to 7 days, and the chemical bath deposition method is a two-step process and often requires an inert environment. The current study reports the synthesis of TiO<sub>2</sub>@SnS<sub>2</sub> core–shell nanocomposites using a thermal decomposition method with a shorter synthesis time (60 min) without the need of an inert

environment. The TiO<sub>2</sub>@SnS<sub>2</sub> core–shell nanocomposites were first characterized using various techniques and then they were explored for their photocatalytic activity towards the photodegradation of CV.

## 2 Experimental

### 2.1 Materials

Titanium isopropoxide (TIP) (97%, Sigma-Aldrich), SnCl<sub>4</sub>·5H<sub>2</sub>O (98%, Sigma-Aldrich), thiourea (98%, SRL Chemicals), methanol (MeOH) (99%, Rankem), acetonitrile (99.5%, Rankem), dodecylamine (DDA) (99%, Rankem), sodium hydroxide (99%, Rankem), diphenyl ether (DPE, 99%, Sigma-Aldrich) and crystal violet (CV, 97%, Sigma-Aldrich) were used.

### 2.2 Preparation of materials

**2.2.1 Synthesis of TiO<sub>2</sub> microspheres.** TiO<sub>2</sub> microspheres were prepared using a reported wet chemical method.<sup>68</sup> Typically, 0.18 mL of H<sub>2</sub>O and 0.345 mL of dodecyl amine (DDA) were taken in a mixture of solvents (100 mL of methanol and 50 mL of acetonitrile) and the contents were stirred for 10 min. After this, 1 mL of titanium isopropoxide was added and the reaction mixture was further stirred for about 6 h at room temperature. The contents were centrifuged, and the collected product was washed with MeOH and dried in an oven at 60 °C for 12 h to obtain as-prepared TiO<sub>2</sub> microspheres. Dodecylamine acts as a surfactant during the synthesis of TiO<sub>2</sub> microspheres. Its hydrophilic amine group interacts with polar solvent molecules (methanol), while the hydrophobic tail interacts with non-polar titanium isopropoxide. During the hydrolysis and condensation of TIP, it forms TiO<sub>2</sub> nuclei. The hydrophobic tail of DDA binds to TiO<sub>2</sub> particles *via* van der Waals forces preventing agglomeration. This stabilizes the dispersion, lowers surface energy, and leads to controlled nucleation and growth, resulting in uniform TiO<sub>2</sub> microspheres.<sup>69,70</sup> The as-prepared TiO<sub>2</sub> microspheres were calcined at 500 °C for 3 h (heating rate = 2° min<sup>-1</sup>) to obtain calcined TiO<sub>2</sub> microspheres. The calcined TiO<sub>2</sub> microspheres were surface-modified using NaOH.<sup>71</sup> For this, 100 mg of calcined TiO<sub>2</sub> microspheres were added to 10 mL of 5 M NaOH aqueous solution and left at room temperature for about 24 h. The contents were centrifuged, washed with de-ionised water and with 0.1 N HCl solution. The sample was dried in an oven at 60 °C for 12 h to obtain NaOH-modified TiO<sub>2</sub> microspheres (TiO<sub>2</sub>–NaOH).

Zeta potential measurements were done for calcined TiO<sub>2</sub> and NaOH-modified TiO<sub>2</sub>. The surface charge as measured from the zeta potential analyzer was +10.1 mV and -11.8 mV for TiO<sub>2</sub>–calc. and TiO<sub>2</sub>–NaOH, respectively. The change in surface charge from positive to negative indicates successful surface modification of TiO<sub>2</sub> microspheres with NaOH.

### 2.2.2 Synthesis of TiO<sub>2</sub>@SnS<sub>2</sub> core–shell nanocomposites.

To synthesize TiO<sub>2</sub>@SnS<sub>2</sub> core–shell nanocomposites, 100 mg of TiO<sub>2</sub>–NaOH microspheres were taken in 10 mL of DPE in a 50 mL RB flask. The contents were sonicated for one min followed by addition of  $x$  mmol of SnCl<sub>4</sub>·5H<sub>2</sub>O and  $2x$  mmol of



Table 1 Synthetic details of  $\text{TiO}_2@\text{SnS}_2$  core–shell nanocomposites and their sample codes

Sample code	$\text{TiO}_2\text{-NaOH}$ (mg)	$\text{SnCl}_4\cdot 5\text{H}_2\text{O}$ (mmol)	Thiourea (mmol)	Solvent	Reaction temperature (°C)	Reaction time (min)
$\text{SnS}_2$	—	0.50	1.0	Diphenyl ether	$200 \pm 2$	$60 \pm 5$
$\text{TiO}_2\text{-SnS}_2\text{-0.05}$	100	0.05	0.1	Diphenyl ether	$200 \pm 2$	$60 \pm 5$
$\text{TiO}_2\text{-SnS}_2\text{-0.1}$	100	0.10	0.2	Diphenyl ether	$200 \pm 2$	$60 \pm 5$
$\text{TiO}_2\text{-SnS}_2\text{-0.15}$	100	0.15	0.3	Diphenyl ether	$200 \pm 2$	$60 \pm 5$

thiourea (Table 1). After refluxing the reaction mixture for about 60 min in air at about 200 °C, the contents were allowed to cool to RT, followed by the addition of about 20 mL of MeOH. The obtained brown precipitate was centrifuged and washed (2–3 times) with methanol. The precipitate was dried in a vacuum desiccator overnight to obtain the  $\text{TiO}_2@\text{SnS}_2$  core–shell nanocomposite. Pure  $\text{SnS}_2$  nanoparticles were also synthesized using a similar synthetic approach in the absence of  $\text{TiO}_2\text{-NaOH}$  microspheres.

### 2.3 Photocatalytic studies

Crystal violet is toxic and carcinogenic with a complex structure and is widely used in textiles, microbiological staining, printing, *etc.*, and leads to water pollution. CV is a cationic triphenylmethane dye which is highly resistant to natural degradation.

All the photodegradation experiments were done under sunlight irradiation between 1 PM and 2 PM at Indian Institute of Technology Roorkee, Roorkee, India between March 2024 and May 2024. The solar irradiance data were obtained using the average solar data sourced from ProfileSolar.<sup>72</sup> The average intensity of the sun during spring (March–May) is about 6.62 kWh per  $\text{m}^2$  per day, *i.e.*, 276 W  $\text{m}^{-2}$   $\text{h}^{-1}$ . The photocatalytic experiments were done by taking 5 mg each of  $\text{TiO}_2@\text{SnS}_2$  core–shell nanocomposites in 5 mL of CV aqueous solution ( $2 \times 10^{-5}$  M) in a test tube followed by sonication for one minute. The adsorption–desorption equilibrium was achieved by keeping the mixture in the dark for about 30 min. After that, the contents were exposed to sunlight for 60 min. The contents were centrifuged to remove the photocatalyst and the supernatant solutions were analysed using UV-Vis spectroscopy. A blank experiment (*i.e.*, no catalyst) was also carried out to understand the self-degradation of crystal violet under sunlight. The % degradation of crystal violet was estimated using the following formula:

$$\text{Degradation\%} = (1 - C_t/C_0) \times 100$$

where  $C_0$  and  $C_t$  denote the concentration of crystal violet at adsorption equilibrium and at any irradiation time ' $t$ ', respectively.

### 2.4 Characterization

Powder X-ray diffraction (XRD) measurements were carried out for phase identification using a Rigaku Miniflex 600 powder X-ray diffractometer ( $\text{Cu-K}\alpha$ ,  $\lambda = 1.5406 \text{ \AA}$ ). A Thermo Nicolet FT-IR spectrophotometer was used for recording FT-IR spectra of the

samples in the range of 4000–400  $\text{cm}^{-1}$  using KBr pellets. For thermogravimetric analysis (TGA), a PerkinElmer Pyris Diamond instrument was employed in the temperature range of 30–1000 °C (heating rate = 10 °C  $\text{min}^{-1}$ ) in air. The morphological and EDX analyses of the samples were done using a Thermo Fisher Apreo field emission SEM (operating voltage = 20 kV). TEM measurements were done using a Thermo Fisher TALOS F200X transmission electron microscope (operating voltage = 200 kV). For the TEM analysis, 1 mg of each sample was taken in a test tube to which 5 mL of ethanol was added. The mixture was sonicated for about 45 min and then drop-cast over a copper grid followed by drying overnight at room temperature. HRTEM images and SAED patterns of the nanocomposites were recorded using the same instrument. EDS line scan and elemental mapping of the nanocomposites were recorded using a JEOL JEM-3200FS transmission electron microscope (operating voltage = 300 kV; energy resolution = 127 eV). The measurements were performed by carefully optimizing the acquisition parameters, such as beam current and dwell time, to minimize beam effects and no significant beam-induced sample damage was observed during the EDS measurements. The oxidation states of the elements present in the  $\text{TiO}_2@\text{SnS}_2$  core–shell nanocomposites were determined using a Physical Electronics PHI 5000 Versa Probe III XPS spectrometer using  $\text{Al-K}\alpha$  radiation ( $\lambda = 1486.6 \text{ eV}$ ). The optical studies on the core–shell nanocomposites were done using a Cary 5000 UV-Vis-NIR spectrophotometer in the reflectance mode in the wavelength range 300 nm to 800 nm. A diffuse reflectance accessory was used for this purpose. About 10 mg of each sample powder was used to measure the reflectance spectra. The specific surface area of the samples was measured *via*  $\text{N}_2$  physisorption at 77 K on a Nova 2200e Quantachrome instrument using the BET method. A Shimadzu UV-2600 UV-Vis spectrophotometer was used for recording absorption spectra during the photodegradation studies. Photoluminescence (PL) spectral measurements were made using a Fluoromax-4 spectrophotofluorometer at room temperature. 1 mg of sample powder was dispersed in about 3 mL of deionized water by sonication and PL spectra were recorded for the dispersion with an excitation wavelength of 450 nm.

## 3 Results and discussion

### 3.1 X-ray diffraction

The powder XRD patterns of calcined  $\text{TiO}_2$  (before NaOH modification) and  $\text{TiO}_2$  (after modification with NaOH) are displayed in Fig. S1. The XRD patterns of both the samples show



peaks at similar  $2\theta$  values and match with that of anatase  $\text{TiO}_2$  (JCPDS file no. 84-1286) indicating that there is no change in the  $\text{TiO}_2$  phase after modification with  $\text{NaOH}$ . The XRD patterns of  $\text{TiO}_2\text{-NaOH}$ ,  $\text{SnS}_2$  nanoparticles and  $\text{TiO}_2\text{@SnS}_2$  core–shell nanocomposites are displayed in Fig. 1. The XRD pattern of  $\text{TiO}_2\text{-NaOH}$  microspheres shows peaks at  $2\theta = 25.39^\circ$ ,  $36.96^\circ$ ,  $37.93^\circ$ ,  $38.76^\circ$ ,  $48.02^\circ$ ,  $53.94^\circ$ ,  $55.19^\circ$ ,  $62.74^\circ$ ,  $68.93^\circ$ ,  $70.39^\circ$ ,  $75.14^\circ$  and  $76.2^\circ$  which correspond to (101), (103), (004), (112), (200), (105), (211), (204), (116), (220), (215) and (301) planes, respectively, of the anatase phase of  $\text{TiO}_2$ . The XRD pattern of  $\text{SnS}_2$  nanoparticles shows peaks at  $2\theta = 28.32^\circ$ ,  $32.16^\circ$ ,  $41.83^\circ$ ,  $45.94^\circ$ ,  $50.04^\circ$ ,  $52.51^\circ$ ,  $58.48^\circ$ ,  $60.76^\circ$ ,  $63.05^\circ$ ,  $67.30^\circ$  and  $70.48^\circ$  indexed to (100), (011), (012), (003), (110), (111), (200), (201), (004), (202) and (113) planes, respectively, of the Berndtite-2T phase of hexagonal  $\text{SnS}_2$  (JCPDS file no. 83-1705). The powder XRD patterns of  $\text{TiO}_2\text{@SnS}_2$  core–shell nanocomposites ( $\text{TiO}_2\text{-SnS}_2\text{-0.05}$ ,  $\text{TiO}_2\text{-SnS}_2\text{-0.1}$  and  $\text{TiO}_2\text{-SnS}_2\text{-0.15}$ ) show peaks due to the anatase phase of  $\text{TiO}_2$  and also show peaks at  $2\theta = 28.59^\circ$  and  $50.35^\circ$  due to (100) and (110) planes of the Berndtite-2T phase of hexagonal  $\text{SnS}_2$ . It is known that the crystallite coherence and stacking faults of nanoparticles may influence the activity.<sup>73</sup> The crystallite size of  $\text{SnS}_2$  nanoparticles was estimated from the XRD patterns of  $\text{SnS}_2$ ,  $\text{TiO}_2\text{-SnS}_2\text{-0.05}$ ,  $\text{TiO}_2\text{-SnS}_2\text{-0.1}$  and  $\text{TiO}_2\text{-SnS}_2\text{-0.15}$  and the values are 11.6 nm, 10.2 nm, 8.8 nm and 8.4 nm, respectively. The crystallite size of  $\text{TiO}_2$  was estimated from the XRD patterns of  $\text{TiO}_2\text{-NaOH}$ ,  $\text{TiO}_2\text{-SnS}_2\text{-0.05}$ ,  $\text{TiO}_2\text{-SnS}_2\text{-0.1}$ , and  $\text{TiO}_2\text{-SnS}_2\text{-0.15}$  and the values are 16.2 nm, 15.9 nm, 15.1 nm, and 14.4 nm, respectively.

The dislocation density and crystallite strain for  $\text{TiO}_2$  and  $\text{SnS}_2$  were estimated for the  $\text{TiO}_2\text{@SnS}_2$  core–shell nanocomposites. Dislocation density ( $\rho$ ) is defined as the number of dislocation lines per unit volume and is estimated using eqn. (1).<sup>74</sup>

$$\rho = (1/D^2) \quad (1)$$

where  $D$  is the crystallite size.

The dislocation density values for  $\text{SnS}_2$  in  $\text{SnS}_2$ ,  $\text{TiO}_2\text{-SnS}_2\text{-0.05}$ ,  $\text{TiO}_2\text{-SnS}_2\text{-0.1}$  and  $\text{TiO}_2\text{-SnS}_2\text{-0.15}$  are  $0.0074 \text{ nm}^{-2}$ ,  $0.0096$

$\text{nm}^{-2}$ ,  $0.0129 \text{ nm}^{-2}$ , and  $0.014 \text{ nm}^{-2}$ , respectively. The dislocation density values for  $\text{TiO}_2$  in  $\text{TiO}_2\text{-NaOH}$ ,  $\text{TiO}_2\text{-SnS}_2\text{-0.05}$ ,  $\text{TiO}_2\text{-SnS}_2\text{-0.1}$  and  $\text{TiO}_2\text{-SnS}_2\text{-0.15}$  are  $0.0038 \text{ nm}^{-2}$ ,  $0.0039 \text{ nm}^{-2}$ ,  $0.0043 \text{ nm}^{-2}$ , and  $0.0048 \text{ nm}^{-2}$ , respectively. The dislocation density of both  $\text{TiO}_2$  and  $\text{SnS}_2$  lattices is small. This suggests a high degree of crystallinity of  $\text{TiO}_2\text{-NaOH}$ ,  $\text{SnS}_2$ , and  $\text{TiO}_2\text{@SnS}_2$  core–shell nanocomposites. Also, the dislocation density increases as the thickness of the shell in the core–shell nanocomposites increases. Crystallite strain is defined as the small distortion in the crystal lattice due to defects or dislocations, causing a slight variation in atomic positions. Due to this, broadening of XRD peaks is observed without change in peak positions. The crystallite strain was estimated using eqn. (2).<sup>75</sup>

$$\beta \cos \theta = K\lambda/D + 4\epsilon \sin \theta \quad (2)$$

where  $\epsilon$  is the crystallite strain (or microstrain) and is determined from the slope of linear fit of the plot between  $\beta \cos \theta$  and  $4 \sin \theta$ , commonly known as the Williamson–Hall plot. Fig. S2 provides the Williamson–Hall plots for  $\text{TiO}_2\text{-NaOH}$  and  $\text{TiO}_2\text{@SnS}_2$  core–shell nanocomposites. The crystallite strain ( $\epsilon$ ) values for  $\text{TiO}_2\text{-NaOH}$ ,  $\text{TiO}_2\text{-SnS}_2\text{-0.05}$ ,  $\text{TiO}_2\text{-SnS}_2\text{-0.1}$  and  $\text{TiO}_2\text{-SnS}_2\text{-0.15}$  are  $0.00378$ ,  $0.00395$ ,  $0.00432$ , and  $0.00468$ , respectively. There is an increase in crystallite strain as shell ( $\text{SnS}_2$ ) thickness increases. The presence of more number of dislocation lines/defects (dislocation density) leads to higher microstrain in the lattice.<sup>76,77</sup> The crystallite strain for  $\text{SnS}_2$  could not be estimated as there are only two peaks due to  $\text{SnS}_2$  in the XRD patterns of  $\text{TiO}_2\text{@SnS}_2$  core–shell nanocomposites.

The  $\text{TiO}_2$  microspheres (as prepared) were calcined at  $750^\circ\text{C}$  and XRD analysis of the sample was performed to confirm the phase of  $\text{TiO}_2$ . The XRD pattern of  $\text{TiO}_2$  calcined at  $500^\circ\text{C}$  matches with the anatase phase of  $\text{TiO}_2$  (JCPDS file no. 84-1286) whereas the XRD pattern of  $\text{TiO}_2$  calcined at  $750^\circ\text{C}$  matches with the rutile phase of  $\text{TiO}_2$  (JCPDS file no. 04-0551) (Fig. S3). This indicates that phase transformation of  $\text{TiO}_2$  from anatase into rutile takes place between  $650^\circ\text{C}$  and  $800^\circ\text{C}$ .

### 3.2 Functional group analysis

The FT-IR spectra of unmodified calcined  $\text{TiO}_2$  microspheres and  $\text{TiO}_2\text{-NaOH}$  are given in Fig. S4. The intensities of IR bands due to OH stretching and bending are more intense in the case of  $\text{TiO}_2\text{-NaOH}$  microspheres compared to unmodified  $\text{TiO}_2$  indicating the successful modification of calcined  $\text{TiO}_2$  microspheres with  $\text{NaOH}$ . The FT-IR spectra of  $\text{TiO}_2\text{-NaOH}$ ,  $\text{SnS}_2$  nanoparticles, and  $\text{TiO}_2\text{@SnS}_2$  core–shell nanocomposites are displayed in Fig. S5. The IR band positions and their assignments for all the samples are given in Table S1. The IR spectrum of  $\text{TiO}_2\text{-NaOH}$  microspheres shows bands at  $3428 \text{ cm}^{-1}$  and  $1637 \text{ cm}^{-1}$  due to the stretching and bending vibration of physisorbed water molecules.<sup>78</sup> The characteristic band due to Ti–O vibration is observed at about  $624 \text{ cm}^{-1}$ .<sup>79</sup> The IR spectra of  $\text{SnS}_2$  nanoparticles and  $\text{TiO}_2\text{@SnS}_2$  core–shell nanocomposites show vibrational bands at about  $3397 \text{ cm}^{-1}$  and  $1638 \text{ cm}^{-1}$  assigned to OH stretching and bending of physisorbed water molecules.<sup>80</sup> The IR bands observed at about  $2925 \text{ cm}^{-1}$ ,  $2852 \text{ cm}^{-1}$  and  $1384 \text{ cm}^{-1}$  are attributed to asymmetric

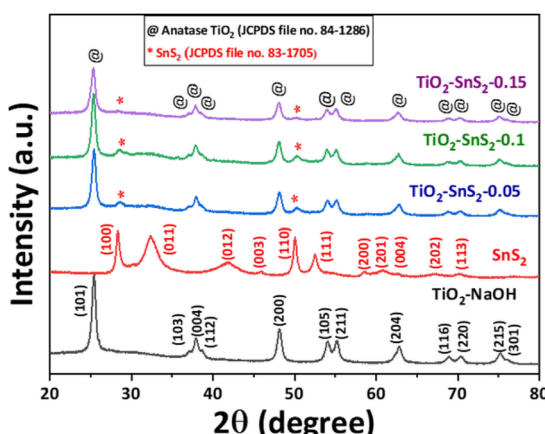


Fig. 1 XRD patterns of  $\text{TiO}_2\text{-NaOH}$ ,  $\text{SnS}_2$  nanoparticles and  $\text{TiO}_2\text{@SnS}_2$  core–shell nanocomposites.



stretching, symmetric stretching and bending vibration of C–H bond, respectively.<sup>81</sup> The IR band at about 1178 cm<sup>−1</sup> corresponds to C–N stretching.<sup>82</sup> The IR spectrum of SnS<sub>2</sub> nanoparticles shows an additional band at 862 cm<sup>−1</sup> assigned to C–H bending.<sup>83</sup> The band at about 611 cm<sup>−1</sup> is assigned to Sn–S stretching.<sup>84</sup>

### 3.3 Thermogravimetric analysis

The TGA curves of TiO<sub>2</sub>–NaOH, SnS<sub>2</sub> nanoparticles, and TiO<sub>2</sub>@SnS<sub>2</sub> core–shell nanocomposites are given in Fig. S6. The DTG plot for TiO<sub>2</sub>–NaOH is given in Fig. S7. The TiO<sub>2</sub>–NaOH microspheres show a two-step weight loss of about 3% in the temperature range of 30–1000 °C. The first weight loss of ~1.3% below 350 °C is due to the loss of physisorbed water molecules.<sup>85</sup> The second weight loss of about 1.7% between 650 °C and 800 °C is due to the loss of chemically bonded OH groups from the surface of TiO<sub>2</sub> (dehydroxylation) and conversion of anatase TiO<sub>2</sub> to rutile phase.<sup>68</sup> The TGA curve of SnS<sub>2</sub> nanoparticles shows a three-step weight loss pattern. The first weight loss of about 3% below 230 °C is due to the loss of surface-adsorbed water molecules. The second weight loss of about 48.5% between 230 °C and 440 °C is attributed to the removal of organic moieties. The third weight loss of about 15.5% is due to oxidation of SnS<sub>2</sub> into SnO<sub>2</sub>.<sup>86</sup> The TiO<sub>2</sub>@SnS<sub>2</sub> core–shell nanocomposites (TiO<sub>2</sub>–SnS<sub>2</sub>-0.05, TiO<sub>2</sub>–SnS<sub>2</sub>-0.1 and TiO<sub>2</sub>–SnS<sub>2</sub>-0.15) show two-step weight loss patterns. The first weight loss of ~3.0%, 3.1% and 3.8%, respectively, observed below 440 °C is due to the loss of physisorbed water molecules and removal of organic moieties. The second weight loss of about 1.9%, 3.4%, and 3.6%, respectively, between 440 °C and 530 °C is attributed to oxidation of SnS<sub>2</sub> into SnO<sub>2</sub>.<sup>87</sup> The TGA studies indicate a total weight loss of about 4.9%, 6.5% and 7.4% in TiO<sub>2</sub>–SnS<sub>2</sub>-0.05, TiO<sub>2</sub>–SnS<sub>2</sub>-0.1, and TiO<sub>2</sub>–SnS<sub>2</sub>-0.15. In the core–shell nanocomposites, the % weight loss due to TiO<sub>2</sub> is negligible and it is primarily due to the presence of SnS<sub>2</sub> in the TiO<sub>2</sub>@SnS<sub>2</sub> core–shell nanocomposites. In the TiO<sub>2</sub>@SnS<sub>2</sub> core–shell nanocomposites, an increase in weight loss is observed with increase in the concentration of SnS<sub>2</sub> nanoparticles (shell) on the TiO<sub>2</sub> core.

### 3.4 FESEM and EDX analyses

The coating of SnS<sub>2</sub> nanoparticles over the TiO<sub>2</sub> microspheres was first done using unmodified as-prepared TiO<sub>2</sub> (*i.e.*, before calcination) and unmodified calcined TiO<sub>2</sub> microspheres. Fig. S8 shows the FESEM images of TiO<sub>2</sub>@SnS<sub>2</sub> nanocomposites synthesized using unmodified as-prepared TiO<sub>2</sub> and unmodified calcined TiO<sub>2</sub> microspheres. The EDX results (Table S2) give distribution of different elements (Ti, O, Sn and S) in the thus prepared TiO<sub>2</sub>@SnS<sub>2</sub> nanocomposites. Both FESEM and EDX results of TiO<sub>2</sub>@SnS<sub>2</sub> nanocomposites, synthesized using as-prepared TiO<sub>2</sub> and unmodified calcined TiO<sub>2</sub> microspheres, indicate non-uniform coating of SnS<sub>2</sub> nanoparticles on the TiO<sub>2</sub> microspheres. Hence, the synthesis of TiO<sub>2</sub>@SnS<sub>2</sub> core–shell nanocomposites was attempted using NaOH-modified TiO<sub>2</sub> microspheres. The SEM images of TiO<sub>2</sub>–NaOH, SnS<sub>2</sub> nanoparticles, and TiO<sub>2</sub>@SnS<sub>2</sub> core–shell nanocomposites, synthesized using TiO<sub>2</sub>–NaOH microspheres as the core, are given in

Fig. S9. The FESEM image of TiO<sub>2</sub>–NaOH microspheres displays spherical particles with a diameter of about 471 ± 17 nm. The FESEM image of SnS<sub>2</sub> nanoparticles shows flake-like morphology. The FESEM images of TiO<sub>2</sub>@SnS<sub>2</sub> core–shell nanocomposites (TiO<sub>2</sub>–SnS<sub>2</sub>-0.05, TiO<sub>2</sub>–SnS<sub>2</sub>-0.1 and TiO<sub>2</sub>–SnS<sub>2</sub>-0.15) show that SnS<sub>2</sub> nanoparticles are uniformly coated over the TiO<sub>2</sub>–NaOH microspheres. The EDX results (Table S3) indicate uniform distribution of different elements (Ti, O, Sn, and S) in all the core–shell nanocomposites. In the TiO<sub>2</sub>@SnS<sub>2</sub> core–shell nanocomposites, an increase in weight% of Sn and S is observed with an increase in [Sn<sup>4+</sup>]:[S<sup>2−</sup>] ratio used during their synthesis.

### 3.5 TEM analysis

The TEM micrographs of TiO<sub>2</sub>–NaOH, SnS<sub>2</sub> nanoparticles, and TiO<sub>2</sub>@SnS<sub>2</sub> core–shell nanocomposites are displayed in Fig. 2. The TiO<sub>2</sub>–NaOH microspheres show spherical morphology with a diameter of about 488 nm. The SnS<sub>2</sub> nanoparticles show flake-like morphology. The flake thickness was estimated using the TEM image. The particle size histogram is shown in Fig. S10, and the mean thickness is about 52 ± 12 nm. The TEM micrographs of TiO<sub>2</sub>@SnS<sub>2</sub> core–shell nanocomposites (TiO<sub>2</sub>–SnS<sub>2</sub>-0.05, TiO<sub>2</sub>–SnS<sub>2</sub>-0.1 and TiO<sub>2</sub>–SnS<sub>2</sub>-0.15) show uniform coating of SnS<sub>2</sub> nanoparticles on the TiO<sub>2</sub> microspheres. Table 2 summarizes the particle diameter, core size and shell thickness observed from the TEM micrographs of TiO<sub>2</sub>@SnS<sub>2</sub> core–shell nanocomposites. The overall diameter of TiO<sub>2</sub>@SnS<sub>2</sub> core–shell nanocomposites varies from 457 nm to 503 nm. The core diameter in the TiO<sub>2</sub>@SnS<sub>2</sub> core–shell nanocomposites varies from 434 nm to 489 nm. The thickness of the shell (SnS<sub>2</sub> nanoparticles) over the TiO<sub>2</sub> microspheres varies from 14 nm to 26 nm. This variation of thickness of the shell is due to the synthetic conditions. Use of different amounts of SnCl<sub>4</sub>·5H<sub>2</sub>O and thiourea during the synthesis of TiO<sub>2</sub>@SnS<sub>2</sub> core–shell nanocomposites leads to variation in shell thickness. The EDS spectrum and elemental analysis data (from TEM measurements) for TiO<sub>2</sub>–SnS<sub>2</sub>-0.15 are given in Fig. S11 and Table S4, respectively. The TEM EDS analysis was performed at three different spots and the results confirm the uniform presence of Ti, Sn, S, and O in the core–shell nanocomposites (TiO<sub>2</sub>–SnS<sub>2</sub>-0.15). The EDS line scanning data and elemental mapping images (from SEM) of TiO<sub>2</sub>@SnS<sub>2</sub> core–shell nanocomposites (TiO<sub>2</sub>–SnS<sub>2</sub>-0.15) are shown in Fig. 3. The EDS line scan (Fig. 3(a)) indicates that the concentration of titanium and oxygen at the edge is less and that of tin and sulfur is high. On moving from the edge to the centre of the particle, the concentration of Ti and O increases and that of Sn and S decreases. The elemental mapping results (Fig. 3(b)) also indicate that Sn and S are predominantly located at the edges of TiO<sub>2</sub> microspheres. On the other hand, Ti and O are present more at the centre. This indicates the successful formation of TiO<sub>2</sub>@SnS<sub>2</sub> core–shell nanocomposites.

The SAED patterns of TiO<sub>2</sub>–NaOH microspheres, SnS<sub>2</sub> nanoparticles, and TiO<sub>2</sub>@SnS<sub>2</sub> core–shell nanocomposites are displayed in Fig. S12. The SAED pattern of TiO<sub>2</sub>–NaOH microspheres shows rings that correspond to the planes of anatase



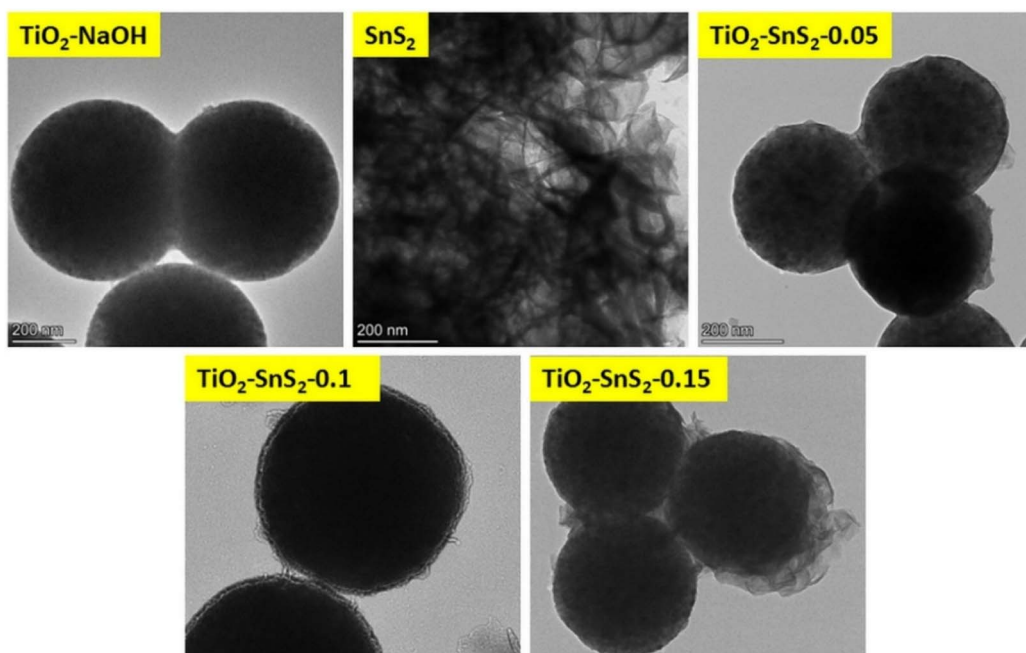


Fig. 2 TEM images of  $\text{TiO}_2$ –NaOH,  $\text{SnS}_2$  nanoparticles and  $\text{TiO}_2$ – $\text{SnS}_2$  core–shell nanocomposites.

Table 2 Summary of results from TEM studies of  $\text{TiO}_2$ – $\text{SnS}_2$  core–shell nanocomposites

Sample code	Particle diameter (nm)	Flake thickness (nm)	Core size (nm)	Shell thickness (nm)
$\text{TiO}_2$ –NaOH	488	—	—	—
$\text{SnS}_2$	—	$52 \pm 12$	—	—
$\text{TiO}_2$ – $\text{SnS}_2$ -0.05	457	—	434	14
$\text{TiO}_2$ – $\text{SnS}_2$ -0.1	478	—	456	21
$\text{TiO}_2$ – $\text{SnS}_2$ -0.15	503	—	489	26

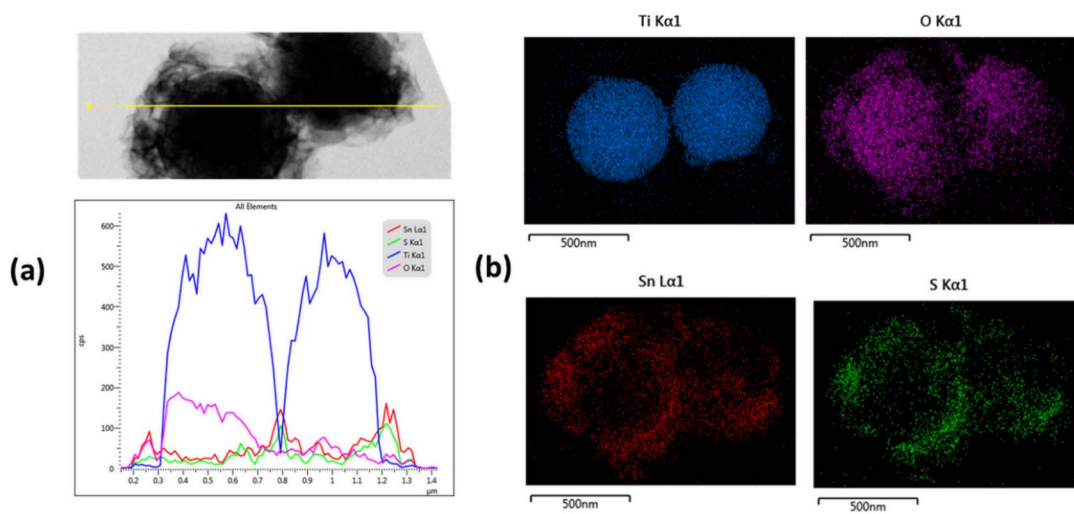


Fig. 3 (a) EDS line scan and (b) elemental mapping data of  $\text{TiO}_2$ – $\text{SnS}_2$ -0.15 core–shell nanocomposite.

$\text{TiO}_2$  (JCPDS file no. 84-1286). The rings, observed in the SAED pattern of  $\text{SnS}_2$  nanoparticles, correspond to the planes of  $\text{SnS}_2$  (JCPDS file no. 83-1705). The SAED patterns of  $\text{TiO}_2$ – $\text{SnS}_2$  core–

shell nanocomposites ( $\text{TiO}_2$ – $\text{SnS}_2$ -0.05,  $\text{TiO}_2$ – $\text{SnS}_2$ -0.1 and  $\text{TiO}_2$ – $\text{SnS}_2$ -0.15) show rings attributed to reflections due to both  $\text{TiO}_2$  and  $\text{SnS}_2$ .

The HRTEM images of  $\text{TiO}_2$ –NaOH microspheres,  $\text{SnS}_2$  nanoparticles, and  $\text{TiO}_2$ @ $\text{SnS}_2$  core–shell nanocomposites are given in Fig. S13. The observed lattice fringes in the HRTEM image of  $\text{TiO}_2$ –NaOH with a *d* spacing of 3.49 Å are attributed to the (101) plane of  $\text{TiO}_2$  (JCPDS file no. 84-1286). The lattice fringes in the HRTEM image of  $\text{SnS}_2$  nanoparticles with a *d* spacing of 3.15 Å is attributed to the (100) plane of  $\text{SnS}_2$  (JCPDS file no. 83-1705). The *d* spacing values (estimated from the lattice fringes) of  $\text{TiO}_2$ @ $\text{SnS}_2$  core–shell nanocomposites ( $\text{TiO}_2$ – $\text{SnS}_2$ -0.05,  $\text{TiO}_2$ – $\text{SnS}_2$ -0.1 and  $\text{TiO}_2$ – $\text{SnS}_2$ -0.15) are 3.49 Å and 3.15 Å attributed to the (101) plane of  $\text{TiO}_2$  and (100) plane of  $\text{SnS}_2$ , respectively. The specific surface area of  $\text{TiO}_2$ –NaOH microspheres,  $\text{SnS}_2$  nanoparticles, and  $\text{TiO}_2$ @ $\text{SnS}_2$  core–shell nanocomposites ( $\text{TiO}_2$ – $\text{SnS}_2$ -0.05,  $\text{TiO}_2$ – $\text{SnS}_2$ -0.1 and  $\text{TiO}_2$ – $\text{SnS}_2$ -0.15), as measured by the BET method, are 9 m<sup>2</sup> g<sup>-1</sup>, 17 m<sup>2</sup> g<sup>-1</sup>, 10 m<sup>2</sup> g<sup>-1</sup>, 13 m<sup>2</sup> g<sup>-1</sup>, and 19 m<sup>2</sup> g<sup>-1</sup>, respectively.

### 3.6 Optical properties

The optical properties of  $\text{TiO}_2$ –NaOH microspheres,  $\text{SnS}_2$  nanoparticles, and  $\text{TiO}_2$ @ $\text{SnS}_2$  core–shell nanocomposites were studied using UV-Vis DRS spectroscopy (Fig. 4) and the Tauc plots (Fig. S14) were used to estimate the band gap. The UV-Vis DRS measurements were done three times for each sample. Table S5 includes error bars for the band gap.<sup>88</sup> The band gap of  $\text{TiO}_2$ –NaOH microspheres and  $\text{SnS}_2$  nanoparticles are 3.1 eV and 2.03 eV, respectively. The  $\text{TiO}_2$ @ $\text{SnS}_2$  core–shell nanocomposites ( $\text{TiO}_2$ – $\text{SnS}_2$ -0.05,  $\text{TiO}_2$ – $\text{SnS}_2$ -0.1 and  $\text{TiO}_2$ – $\text{SnS}_2$ -0.15) have band gaps of 2.23 eV, 2.18 eV and 2.15 eV, respectively. The  $\text{TiO}_2$ @ $\text{SnS}_2$  core–shell nanocomposites exhibit band gap only due to  $\text{SnS}_2$  suggesting that the  $\text{TiO}_2$  microspheres are coated with a thick shell of  $\text{SnS}_2$  nanoparticles. The band gap values were also estimated using K–M plots<sup>89</sup> (Fig. S15) and the values are summarized in Table S5. Although the band gap of a semiconductor can be estimated using both Tauc plots and K–M plots, the band gap values estimated using K–M plots can often be misleading. This is because the K–M function is proportional to the ratio of the absorption and scattering coefficients ( $\alpha$ ) and is considered as an approximate. Furthermore, the K–M

function does not consider the nature of the electronic transition (direct or indirect in a semiconductor).<sup>90</sup>

### 3.7 PL spectroscopy

The PL spectra of  $\text{TiO}_2$ @ $\text{SnS}_2$  core–shell nanocomposites ( $\lambda_{\text{exc}} = 450$  nm) are shown in Fig. 5. The PL spectra of  $\text{TiO}_2$ –NaOH microspheres,  $\text{SnS}_2$  nanoparticles, and  $\text{TiO}_2$ @ $\text{SnS}_2$  core–shell nanocomposites exhibit an emission peak at  $\sim$ 590 nm. This emission peak is due to the recombination of electrons with holes that are trapped above the valence state.<sup>91–93</sup> The emission peak at about 590 nm in  $\text{SnS}_2$  nanoparticles is due to the near band edge emission of the  $\text{SnS}_2$  phase.<sup>94</sup> The order of PL intensity in the samples is:  $\text{TiO}_2$ –NaOH >  $\text{SnS}_2$  >  $\text{TiO}_2$ – $\text{SnS}_2$ -0.05 >  $\text{TiO}_2$ – $\text{SnS}_2$ -0.1 >  $\text{TiO}_2$ – $\text{SnS}_2$ -0.15. The PL intensity is the least for  $\text{TiO}_2$ – $\text{SnS}_2$ -0.15 and it is expected to show the highest photocatalytic activity among all the samples.

### 3.8 XPS analysis

The oxidation states of different elements present in  $\text{TiO}_2$ –NaOH microspheres,  $\text{SnS}_2$  nanoparticles and  $\text{TiO}_2$ @ $\text{SnS}_2$  core–shell nanocomposite ( $\text{TiO}_2$ – $\text{SnS}_2$ -0.15) were determined by XPS analysis, and the results are given in Fig. 6. Table S6 summarizes binding energies of all the elements (Ti, O, Sn and S) present in the samples. As shown in the Ti 2p spectrum of  $\text{TiO}_2$ –NaOH (Fig. 6(a)), the peaks at 456.2 eV and 462.3 eV correspond to  $\text{Ti 2p}_{3/2}$  and  $\text{Ti 2p}_{1/2}$  of  $\text{Ti}^{4+}$ , respectively. The O 1s spectrum of  $\text{TiO}_2$ –NaOH shows peaks at 530.9 eV and 532.1 eV due to lattice oxygen ( $\text{O}^{2-}$ ) and surface hydroxyl (OH) oxygen, respectively.<sup>95,96</sup> The Sn 3d spectrum of  $\text{SnS}_2$  nanoparticles (Fig. 6(b)) shows peaks at 486.0 eV and 494.4 eV due to  $\text{Sn 3d}_{5/2}$  and  $\text{Sn 3d}_{3/2}$  of  $\text{Sn}^{4+}$ , respectively. The S 2p spectrum of  $\text{SnS}_2$  nanoparticles shows peaks at 165.0 eV and 166.2 eV corresponding to  $\text{S 2p}_{3/2}$  and  $\text{S 2p}_{1/2}$ , respectively.<sup>97</sup> The XPS spectrum of the  $\text{TiO}_2$ @ $\text{SnS}_2$  core–shell nanocomposite ( $\text{TiO}_2$ – $\text{SnS}_2$ -0.15) is shown in Fig. 6(c). The Ti 2p spectrum of  $\text{TiO}_2$ – $\text{SnS}_2$ -0.15 shows peaks at 458.0 eV and 463.7 eV attributed to  $\text{Ti 2p}_{3/2}$  and  $\text{Ti 2p}_{1/2}$  of  $\text{Ti}^{4+}$ , respectively. The O 1s spectrum of  $\text{TiO}_2$ – $\text{SnS}_2$ -0.15 shows peaks at 531.0 eV and 532.3 eV assigned to lattice oxygen and surface hydroxyl oxygen, respectively.<sup>95,96</sup> The Sn 3d spectrum of  $\text{TiO}_2$ –

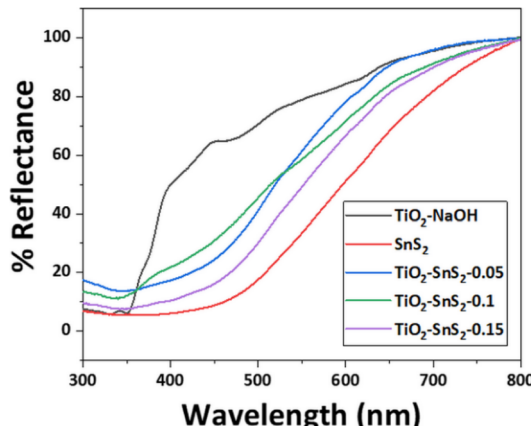


Fig. 4 UV-Vis DRS spectra of  $\text{TiO}_2$ –NaOH,  $\text{SnS}_2$  nanoparticles and  $\text{TiO}_2$ @ $\text{SnS}_2$  core–shell nanocomposites.

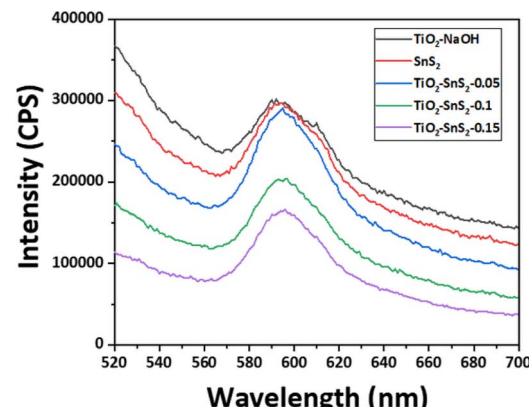
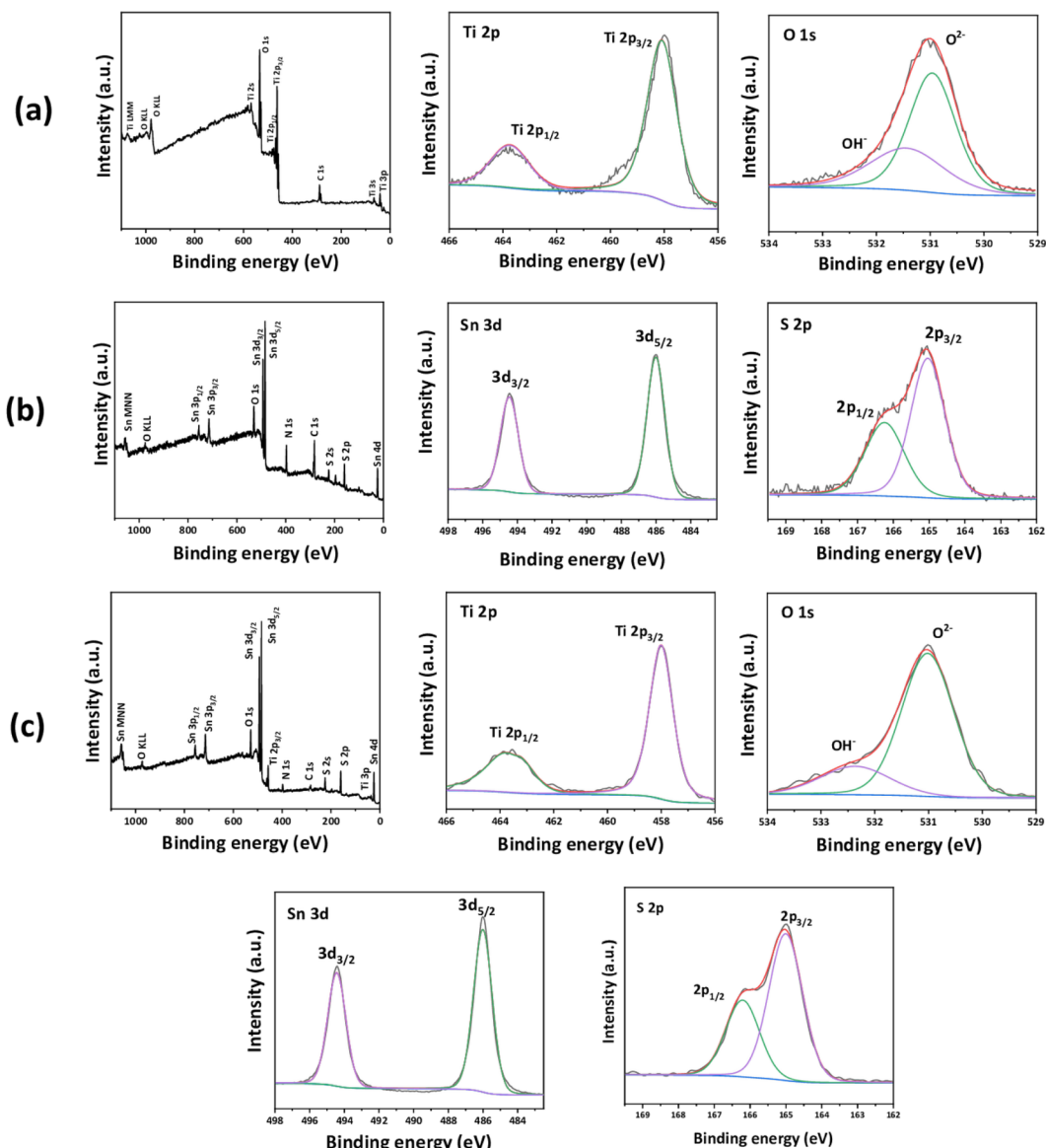


Fig. 5 PL spectra of  $\text{TiO}_2$ –NaOH,  $\text{SnS}_2$  nanoparticles and  $\text{TiO}_2$ @ $\text{SnS}_2$  core–shell nanocomposites.





**Fig. 6** XPS spectra of (a)  $\text{TiO}_2$ -NaOH microspheres, (b)  $\text{SnS}_2$  nanoparticles and (c)  $\text{TiO}_2@ \text{SnS}_2$  core-shell nanocomposite ( $\text{TiO}_2$ - $\text{SnS}_2$ -0.15).

$\text{SnS}_2\text{-0.15}$  shows peaks at 485.9 eV and 494.3 eV due to  $\text{Sn 3d}_{5/2}$  and  $\text{Sn 3d}_{3/2}$  of  $\text{Sn}^{4+}$ , respectively. The S 2p spectrum of  $\text{TiO}_2\text{-SnS}_2\text{-0.15}$  shows peaks at 164.9 eV and 166.2 eV due to  $\text{S 2p}_{3/2}$  and  $\text{S 2p}_{1/2}$ , respectively.<sup>97</sup>

There is a minor decrease in Sn 3d and S 2p binding energy values on going from pure  $\text{SnS}_2$  nanoparticles to the  $\text{TiO}_2@\text{SnS}_2$  core-shell nanocomposites. Also, a minor increase in Ti 2p and O 1s binding energies is observed on going from pure  $\text{TiO}_2$  microspheres ( $\text{TiO}_2\text{-NaOH}$ ) to the core-shell nanocomposites. The shifts in binding energies in the XPS spectrum of the  $\text{TiO}_2@\text{SnS}_2$  core-shell nanocomposite could be due to electron transfer from the core ( $\text{TiO}_2$ ) to the shell ( $\text{SnS}_2$ ) during the formation of the core-shell nanocomposite. The electron transfer leads to a partial positive charge on  $\text{TiO}_2$ , leading to an increase in binding energies of Ti 2p and O 1s and a partial

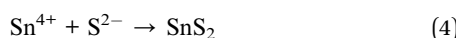
negative charge on  $\text{SnS}_2$ , leading to a decrease in binding energies of Sn 3d and S 2p.<sup>98-100</sup>

To investigate the charge transfer and band (VB and CB) positions in  $\text{TiO}_2@\text{SnS}_2$  core–shell nanocomposites, XPS-VB (UPS spectra) measurements were performed. Fig. S16 provides the XPS-VB spectra of  $\text{TiO}_2$ –NaOH microspheres,  $\text{SnS}_2$  nanoparticles and  $\text{TiO}_2$ – $\text{SnS}_2$ -0.15. The valence band positions estimated from the XPS-VB spectra for  $\text{TiO}_2$ –NaOH microspheres,  $\text{SnS}_2$  nanoparticles and  $\text{TiO}_2$ – $\text{SnS}_2$ -0.15 are 2.83 eV, 1.35 eV and 1.78 eV, respectively. In the  $\text{TiO}_2@\text{SnS}_2$  core–shell nanocomposites, electron transfer occurs from the core ( $\text{TiO}_2$ ) to the shell ( $\text{SnS}_2$ ). The intermediate valence band position of  $\text{TiO}_2$ – $\text{SnS}_2$ -0.15 suggests successful heterostructure formation and interfacial charge transfer between  $\text{TiO}_2$  and  $\text{SnS}_2$ .<sup>101,102</sup> From the optical studies (DRS spectra), the band gaps for  $\text{TiO}_2$ –NaOH and  $\text{SnS}_2$  are 3.1 eV and 2.02 eV, respectively. On applying

the equation,  $E_{CB} = E_{VB} - E_g$ , the conduction band positions of  $\text{TiO}_2\text{-NaOH}$  and  $\text{SnS}_2$  nanoparticles are  $-0.27$  eV and  $-0.67$  eV, respectively. To further confirm the charge transfer in  $\text{TiO}_2\text{@}\text{SnS}_2$  core-shell nanocomposites, EIS measurements were also performed (see Section 3.15 for more details).

### 3.9 Mechanism of formation of $\text{TiO}_2\text{@}\text{SnS}_2$ core-shell nanocomposites

Scheme 1 illustrates the proposed mechanism of formation of  $\text{TiO}_2\text{@}\text{SnS}_2$  core-shell nanocomposites. At first, on surface modification with NaOH, hydroxyl groups are attached on the surface of  $\text{TiO}_2$  microspheres. This can be evidenced from the IR spectral studies (Fig. S4). Due to the presence of hydroxyl groups on the surface of  $\text{TiO}_2$  microspheres,  $\text{Sn}^{4+}$  ions are attached on the surface of  $\text{TiO}_2$  *via* electrostatic interaction. This is followed by the thermal decomposition of thiourea to form  $\text{H}_2\text{S}$  and the formation of  $\text{TiO}_2\text{@}\text{SnS}_2$  core-shell nanocomposites. The reactions involved in the formation of  $\text{SnS}_2$  nanoparticles over  $\text{TiO}_2\text{-NaOH}$  microspheres are given in eqn (3) and (4).<sup>103-105</sup>



$\text{SnS}_2$  nanoflakes are formed by the thermal decomposition of  $\text{SnCl}_4 \cdot 5\text{H}_2\text{O}$  and thiourea in DPE. The formation of nanoflakes is a two-step process, *i.e.*, nucleation followed by growth.<sup>106</sup> At first, tin chloride reacts with thiourea leading to the formation of a small cluster of  $\text{SnS}_2$  (nuclei). The presence of chloride ions leads to oriented growth of particles. The chloride ions adsorbed on the transverse planes of  $\text{SnS}_2$  particles inhibit growth in

those directions. As a result, the growth occurs in the longitudinal axis leading to the formation of  $\text{SnS}_2$  nanoflakes.<sup>82</sup>

### 3.10 Photocatalytic activity

The photocatalytic activity of  $\text{TiO}_2\text{@}\text{SnS}_2$  core-shell nanocomposites was studied using crystal violet as the dye pollutant (see Section 2.3 for more details). As indicated by the UV-Vis spectral results (Fig. 7) on the photodegradation experiments,  $\text{TiO}_2\text{-SnS}_2\text{-0.15}$  achieved about 99% degradation of crystal violet within 60 minutes under sunlight.  $\text{TiO}_2\text{-NaOH}$  microspheres,  $\text{SnS}_2$  nanoparticles,  $\text{TiO}_2\text{-SnS}_2\text{-0.05}$ , and  $\text{TiO}_2\text{-SnS}_2\text{-0.1}$  degrade about 53.1%, 60.2%, 61.5%, and 78.2% of crystal violet, respectively. This indicates that  $\text{TiO}_2\text{-SnS}_2\text{-0.15}$  is a better photocatalyst for the degradation of crystal violet compared to

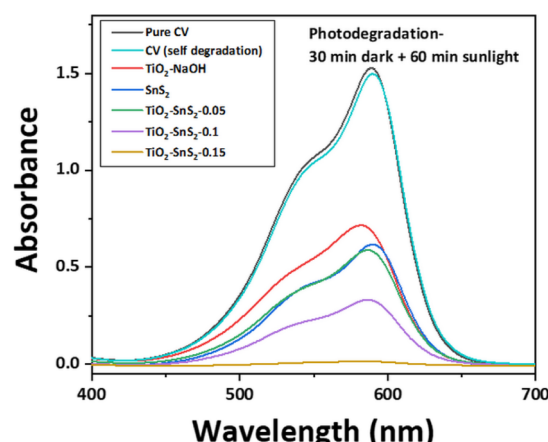
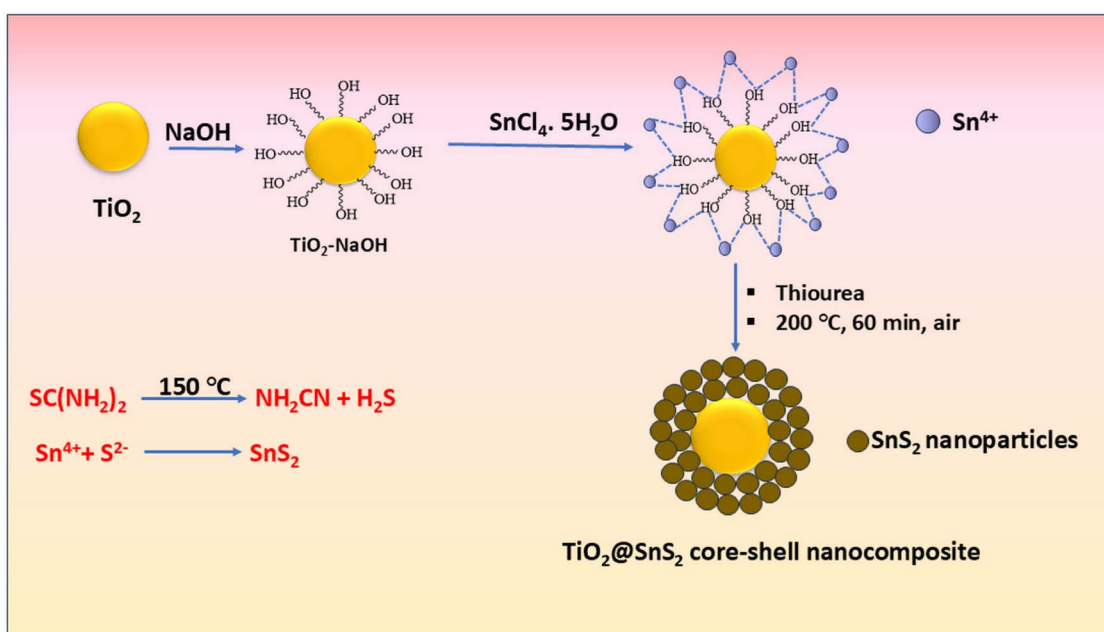


Fig. 7 UV-Vis spectral results indicating the photodegradation of CV using  $\text{TiO}_2\text{@}\text{SnS}_2$  core-shell nanocomposites.



Scheme 1 Mechanism of formation of  $\text{TiO}_2\text{@}\text{SnS}_2$  core-shell nanocomposites.



$\text{TiO}_2$ –NaOH microspheres,  $\text{SnS}_2$  nanoparticles and other core–shell nanocomposites. The self-degradation of crystal violet under sunlight, tested in the absence of any catalyst, was about 1.9%.

Furthermore, dark experiments were carried out in the absence of sunlight to understand adsorption of CV on the  $\text{TiO}_2$ @ $\text{SnS}_2$  core–shell nanocomposites. In this experiment, 5 mg of each catalyst was taken in a test tube to which 5 mL of CV aqueous solution ( $2 \times 10^{-5}$  M) was added. The test tubes were sonicated for one min followed by keeping them in the dark for 30 min/90 min. The UV-Vis absorbance spectra recorded for the supernatant solutions obtained after centrifugation of each mixture are shown in Fig. S17. The % adsorption by  $\text{TiO}_2$ –NaOH microspheres,  $\text{SnS}_2$  nanoparticles and  $\text{TiO}_2$ @ $\text{SnS}_2$  core–shell nanocomposites ( $\text{TiO}_2$ – $\text{SnS}_2$ –0.05,  $\text{TiO}_2$ – $\text{SnS}_2$ –0.1 and  $\text{TiO}_2$ – $\text{SnS}_2$ –0.15) are 15%, 28.1%, 31.3%, 37.9% and 49%, respectively in 30 min and 26%, 47.9%, 34.8%, 39.9% and 53.8%, respectively in 90 min. The adsorption and photodegradation studies indicate that the  $\text{TiO}_2$ @ $\text{SnS}_2$  core–shell nanocomposites act as a good photocatalyst for the degradation of CV and not as an adsorbent.

Furthermore, kinetic experiments were carried out by taking 6 test tubes each containing 5 mg of catalyst ( $\text{TiO}_2$ –NaOH microspheres,  $\text{SnS}_2$  nanoparticles, and  $\text{TiO}_2$ @ $\text{SnS}_2$  core–shell nanocomposites ( $\text{TiO}_2$ – $\text{SnS}_2$ –0.05,  $\text{TiO}_2$ – $\text{SnS}_2$ –0.1 and  $\text{TiO}_2$ – $\text{SnS}_2$ –0.15)) and 5 mL of CV aqueous solution ( $2 \times 10^{-5}$  M). The mixtures were kept in the dark for 30 min which was followed by irradiation with sunlight for different time periods (10–60 min). UV-Vis spectra were recorded for the supernatant solutions obtained after centrifuging the mixture in each test tube.

The kinetics results are shown in Fig. 8(a) and  $\text{TiO}_2$ – $\text{SnS}_2$ –0.15 shows maximum degradation in 60 min. The kinetics of photodegradation of CV by  $\text{TiO}_2$ – $\text{SnS}_2$ –0.15 follows pseudo 1st order kinetics as indicated by  $-\ln(C_t/C_0)$  against irradiation time plots shown in Fig. 8(b). The rate constant values were determined using the kinetic curves. Table 3 summarizes the % adsorption (30 min/90 min), % total degradation (90 min), % photodegradation only, rate constant and  $R^2$  values for  $\text{TiO}_2$ –

NaOH microspheres,  $\text{SnS}_2$  nanoparticles and  $\text{TiO}_2$ @ $\text{SnS}_2$  core–shell nanocomposites ( $\text{TiO}_2$ – $\text{SnS}_2$ –0.05,  $\text{TiO}_2$ – $\text{SnS}_2$ –0.1 and  $\text{TiO}_2$ – $\text{SnS}_2$ –0.15). The rate constant values are in the order:  $\text{TiO}_2$ – $\text{SnS}_2$ –0.15 >  $\text{TiO}_2$ – $\text{SnS}_2$ –0.1 >  $\text{TiO}_2$ – $\text{SnS}_2$ –0.05 >  $\text{SnS}_2$  >  $\text{TiO}_2$ –NaOH indicating that  $\text{TiO}_2$ – $\text{SnS}_2$ –0.15 is the best photocatalyst among all the samples. The better photocatalytic activity of  $\text{TiO}_2$ – $\text{SnS}_2$ –0.15 is attributed to a lower rate of recombination of electron and hole pairs in  $\text{TiO}_2$ – $\text{SnS}_2$ –0.15 as indicated by the PL spectral studies (Fig. 5). The photocatalytic degradation results were compared with those reported in the literature (Table S7).<sup>24,107–128</sup> In the literature, more time (70–390 min) is required for the photodegradation of CV. Wherever lesser time is reported (30–45 min),<sup>116,117</sup> either the amount of catalyst used is high (250 mg/100 mL) or the % photodegradation is less (83–93%). The  $\text{TiO}_2$ @ $\text{SnS}_2$  core–shell nanocomposites (e.g.,  $\text{TiO}_2$ – $\text{SnS}_2$ –0.15), reported in the current work, achieved 99% degradation of CV within 60 minutes under sunlight.

### 3.11 Effect of pH

The photocatalytic degradation efficiency of a catalyst is affected by the pH of the solution. The effect of pH on the photodegradation efficiency of  $\text{TiO}_2$ – $\text{SnS}_2$ –0.15 was studied by varying the pH of the solution between 2 and 10. The pH of the solutions was varied using 0.1 M HCl and 0.1 M NaOH. The experiment was performed by taking 5 mg of catalyst ( $\text{TiO}_2$ – $\text{SnS}_2$ –0.15) in 5 mL of CV aqueous solution ( $2 \times 10^{-5}$  M) at different pH values (2–10) in different test tubes. The contents were kept in the dark (for 30 min) followed by irradiation with sunlight for 60 min and UV-Vis absorbance spectra were measured for the supernatant solutions obtained after centrifugation. The variation of the photodegradation efficiency of  $\text{TiO}_2$ – $\text{SnS}_2$ –0.15 with pH is shown in Fig. S18(a). The results indicate that maximum photocatalytic efficiency is observed at pH = 7.

At lower pH, there are more  $\text{H}^+$  ions in the solution that make the surface of the catalyst positively charged (zeta potential = + 19.0 mV at pH = 4). Crystal violet is a cationic dye, and it will experience electrostatic repulsion towards the surface

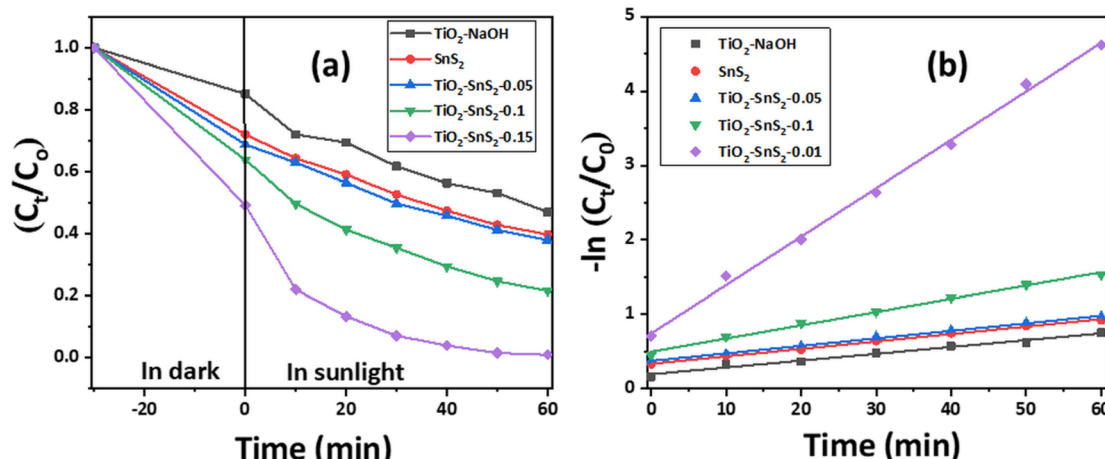


Fig. 8 (a)  $(C_t/C_0)$  plots and (b)  $-\ln(C_t/C_0)$  vs. time plots for  $\text{TiO}_2$ –NaOH microspheres,  $\text{SnS}_2$  nanoparticles and  $\text{TiO}_2$ @ $\text{SnS}_2$  core–shell nanocomposites as the catalyst for the photodegradation of CV.



Table 3 Photocatalytic degradation results of crystal violet using  $\text{TiO}_2@\text{SnS}_2$  core–shell nanocomposites

Sample code	% Adsorption (30 min)	% Adsorption (90 min)	Total degradation% (30 min dark + 60 min sunlight)	Photodegradation% only (60 min)	Rate constant for photodegradation ( $\text{min}^{-1}$ )	$R^2$
$\text{TiO}_2\text{-NaOH}$	15.0	26.0	53.1	38.1	$9.1 \times 10^{-3}$	0.98
$\text{SnS}_2$	28.1	47.9	60.2	32.1	$9.5 \times 10^{-3}$	0.98
$\text{TiO}_2\text{-SnS}_2\text{-0.05}$	31.3	34.8	61.5	30.2	$1.0 \times 10^{-2}$	0.99
$\text{TiO}_2\text{-SnS}_2\text{-0.1}$	37.9	39.9	78.2	38.3	$1.7 \times 10^{-2}$	0.99
$\text{TiO}_2\text{-SnS}_2\text{-0.15}$	49.0	53.8	99.0	50.0	$6.4 \times 10^{-2}$	0.99

of the catalyst in an acidic medium leading to a decrease in the photocatalytic efficiency. On the other hand, in basic medium, the presence of more  $\text{OH}^-$  ions in the solution will lead to a negatively charged catalyst surface (zeta potential =  $-21.4 \text{ mV}$  at  $\text{pH} = 10$ ). This results in an electrostatic attraction towards crystal violet leading to higher photodegradation efficiency by the catalyst.<sup>129</sup>

### 3.12 Effect of catalyst dosage

To determine the optimum amount of catalyst required to degrade CV using  $\text{TiO}_2@\text{SnS}_2$  core–shell nanocomposites, the effect of catalyst dosage on the photodegradation efficiency was studied. The catalyst ( $\text{TiO}_2\text{-SnS}_2\text{-0.15}$ ) was taken in different amounts ( $1\text{--}8 \text{ mg}$ ) in  $5 \text{ mL}$  of aqueous CV solution ( $2 \times 10^{-5} \text{ M}$ ) in test tubes. The mixtures were kept in the dark (for 30 min) followed by sunlight irradiation for 60 min and the UV-Vis absorbance spectra were measured for the supernatant solutions obtained after centrifugation. The UV-Vis spectral results shown in Fig. S18(b) indicate that  $5 \text{ mg}$  of  $\text{TiO}_2\text{-SnS}_2\text{-0.15}$  in  $5 \text{ mL}$  of CV is the optimum catalyst dosage for the photodegradation of CV.<sup>130</sup>

### 3.13 Scavenger tests

To understand the mechanism of photodegradation of CV by  $\text{TiO}_2\text{-SnS}_2\text{-0.15}$ , scavenger tests were performed. Different scavengers (isopropyl alcohol (IPA), ammonium oxalate (AO) and *p*-benzoquinone (PBQ)) were used to trap  $\text{OH}^\cdot$ ,  $\text{O}_2^\cdot^-$  and  $\text{h}^\cdot$ , respectively.<sup>127,131</sup> In a typical experiment,  $10 \text{ mM}$  of scavenger was added to  $5 \text{ mL}$  aqueous solution of CV ( $2 \times 10^{-5} \text{ M}$ ) followed by the addition of  $5 \text{ mg}$  of catalyst ( $\text{TiO}_2\text{-SnS}_2\text{-0.15}$ ). The contents were kept in the dark (for 30 min) followed by irradiation with sunlight for 60 min and UV-Vis absorbance spectra were measured for the supernatant solutions obtained after centrifugation. The scavenger test results (Fig. S19) show a decrease of about 15.2%, 39.4% and 53.4% in the presence of IPA, PBQ, and AO, respectively. This indicates that  $\text{O}_2^\cdot^-$  and  $\text{h}^\cdot$  are the major species responsible for the photodegradation of CV using  $\text{TiO}_2@\text{SnS}_2$  core–shell nanocomposites as the catalyst.

### 3.14 Mechanism of photodegradation of crystal violet

Crystal violet degrades *via* two different pathways, *i.e.*, *N*-demethylation and oxidative degradation.<sup>106,132</sup> In the first case, reactive oxygen species (ROS) attack the *N,N*-dimethyl groups of the CV molecules leading to the formation of *N*-de-methylated CV species. In the second case, the ROS species attack the

central carbon of CV facilitated by its conjugated amino-triphenylmethane structure leading to disruption in the conjugation and decolourisation of CV. This step leads to the formation of intermediates such as 4-(*N,N*-dimethylamino)-4'-(*N,N*-dimethylamino)benzophenone and 4-(*N,N*-dimethylamino)phenol. Both these steps can occur simultaneously or one-by-one.<sup>132</sup> The formed intermediates undergo further oxidation leading to ring opening and complete mineralisation of CV leading to formation of  $\text{CO}_2$  and  $\text{H}_2\text{O}$ .<sup>133</sup>

Scheme 2 gives the proposed mechanism of photodegradation of crystal violet in the presence of  $\text{TiO}_2@\text{SnS}_2$  core–shell nanocomposites as the catalyst. The valence band (VB) and conduction band (CB) positions of  $\text{TiO}_2$  are located at  $2.83 \text{ eV}$  and  $-0.27 \text{ eV}$ , respectively.<sup>134</sup> The VB and CB of  $\text{SnS}_2$  are located at  $1.35 \text{ eV}$  and  $-0.67 \text{ eV}$ , respectively,<sup>46</sup> indicating a more negative band potential than that of  $\text{TiO}_2$  (see Section 3.8, XPS-VB results).

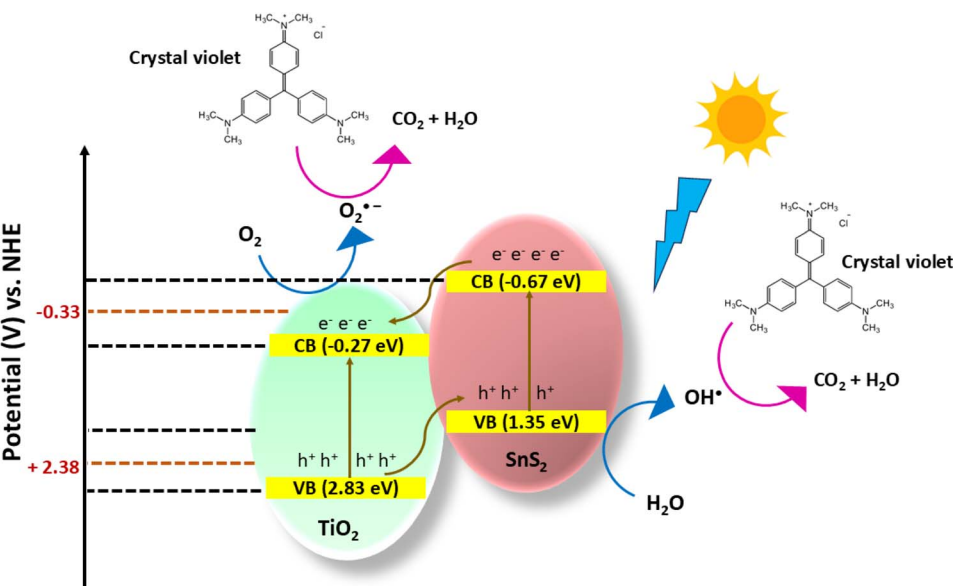
Upon irradiation with sunlight, electrons in the VB of  $\text{SnS}_2$  are excited to its CB, leaving behind photogenerated holes. Due to the favourable band alignment, the excited electrons in the CB of  $\text{SnS}_2$  migrate to the CB of  $\text{TiO}_2$ , while the holes in the VB of  $\text{TiO}_2$  migrate to that of  $\text{SnS}_2$ . This charge transfer effectively suppresses electron–hole recombination, enhancing the photocatalytic activity. The electrons in the CB of  $\text{TiO}_2$  interact with dissolved  $\text{O}_2$  molecules to generate superoxide radicals ( $\text{O}_2^\cdot^-$ ), while the holes in the VB of  $\text{SnS}_2$  oxidize water molecules to produce  $\text{OH}^\cdot$ . These highly reactive species then attack and degrade crystal violet molecules into harmless end products ( $\text{CO}_2$  and  $\text{H}_2\text{O}$ ).<sup>129,135,136</sup>

The standard potential for  $\text{O}_2/\text{O}_2^\cdot^-$  is  $-0.33 \text{ V}$  and that for  $\text{OH}^\cdot/\text{OH}^\cdot$  is  $2.38 \text{ V}$ . The VB of  $\text{TiO}_2$  ( $2.83 \text{ V}$ ) is more positive than that of  $\text{OH}^\cdot/\text{OH}^\cdot$  ( $2.38 \text{ V}$ ) indicating that  $\text{OH}^\cdot$  could be generated. Similarly, the conduction band of  $\text{SnS}_2$  ( $-0.67 \text{ V}$ ) is more negative than that of  $\text{O}_2/\text{O}_2^\cdot^-$  ( $-0.33 \text{ V}$ ) indicating that  $\text{O}_2^\cdot^-$  could also be generated. The generation of both  $\text{OH}^\cdot$  and  $\text{O}_2^\cdot^-$  by  $\text{TiO}_2@\text{SnS}_2$  core–shell nanocomposites on solar irradiation leads to the degradation of crystal violet into  $\text{CO}_2$  and  $\text{H}_2\text{O}$  as shown in Scheme 2.

### 3.15 EIS studies

Electrochemical Impedance Spectroscopy (EIS) measurements were performed for  $\text{TiO}_2\text{-NaOH}$ ,  $\text{SnS}_2$  nanoparticles and  $\text{TiO}_2@\text{SnS}_2$  core–shell nanocomposites ( $\text{TiO}_2\text{-SnS}_2\text{-0.05}$ ,  $\text{TiO}_2\text{-SnS}_2\text{-0.1}$  and  $\text{TiO}_2\text{-SnS}_2\text{-0.15}$ ) to understand the charge separation. The samples were deposited onto FTO (fluorine-doped tin oxide) glass substrates (dimensions:  $1 \text{ cm} \times 2 \text{ cm}$ ). For each





Scheme 2 Mechanism of photodegradation of crystal violet using  $\text{TiO}_2@\text{SnS}_2$  core–shell nanocomposites as the catalyst.

sample, 30 mg of the sample ( $\text{TiO}_2\text{-NaOH}$ ,  $\text{SnS}_2$  nanoparticles and  $\text{TiO}_2@\text{SnS}_2$  core–shell nanocomposites) was dispersed in 3 mL of ethanol to form a homogeneous slurry. The mixture was subjected to sonication for 45 minutes to ensure uniform dispersion. Subsequently, the slurry was drop-cast onto the FTO substrates and dried in an oven (at  $\sim 50^\circ\text{C}$ ).

The electrochemical measurements were conducted using a conventional three-electrode system. The modified FTO glass slides (coated with  $\text{TiO}_2\text{-NaOH}$ ,  $\text{SnS}_2$  and  $\text{TiO}_2@\text{SnS}_2$  core–shell nanocomposites) served as the working electrode.  $\text{Ag}/\text{AgCl}$  electrode was employed as the reference electrode. A platinum wire was employed as the counter electrode. The EIS measurements were performed in 0.1 M KOH aqueous solution as the electrolyte, over a frequency range of 0.1 Hz to 100 kHz (Multi Autolab/M204 electrochemical workstation (Metrohm Autolab B.V., Netherlands)).

Fig. S20 provides the Nyquist plots for all the samples. The order of arc radius is as follows:  $\text{TiO}_2\text{-NaOH} > \text{SnS}_2 > \text{TiO}_2\text{-SnS}_2\text{-0.05} > \text{TiO}_2\text{-SnS}_2\text{-0.1} > \text{TiO}_2\text{-SnS}_2\text{-0.15}$ . The arc radius in the Nyquist plot corresponds to charge transfer resistance ( $R_{\text{ct}}$ ) at the interface of the electrode and electrolyte.<sup>137</sup> A smaller arc radius indicates lower charge-transfer resistance ( $R_{\text{ct}}$ ), which suggests faster interfacial charge transfer. The smaller arc radius observed in  $\text{TiO}_2\text{-SnS}_2\text{-0.15}$  among all the samples suggests faster interfacial charge transfer and thus its better photocatalytic efficiency towards degradation of crystal violet compared to the other samples.

### 3.16 Time resolved PL decay experiments

PL decay experiments were performed using an FLS-1000-xs-t (Edinburgh Instruments) system for  $\text{TiO}_2\text{-NaOH}$  microspheres,  $\text{SnS}_2$  nanoparticles, and  $\text{TiO}_2@\text{SnS}_2$  core–shell nanocomposites ( $\text{TiO}_2\text{-SnS}_2\text{-0.05}$ ,  $\text{TiO}_2\text{-SnS}_2\text{-0.1}$  and  $\text{TiO}_2\text{-SnS}_2\text{-0.15}$ ) and the data are presented in Fig. S21. The excitation and

emission wavelengths were 450 nm and 590 nm, respectively. The PL decay curves were well fitted according to the bi-exponential function in the form of  $R(t) = A + B_1 \exp(-t/\tau_1) + B_2 \exp(-t/\tau_2)$ .

Where,  $A$  is a constant background offset,  $B_1$  and  $B_2$  are amplitude coefficients of the two decay components,  $\tau_1$  is the lifetime of the faster decay component and  $\tau_2$  is the lifetime of the slower decay component.

The average lifetime  $\tau_{\text{avg}}$  was calculated using the formula  $\tau_{\text{avg}} = (B_1 \tau_1^2 + B_2 \tau_2^2) / (B_1 \tau_1 + B_2 \tau_2)$ .<sup>138</sup> Table S8 summarizes the fluorescence decay components for all the samples. The average lifetime ( $\tau_{\text{avg}}$ ) values estimated for  $\text{TiO}_2\text{-NaOH}$  microspheres,  $\text{SnS}_2$  nanoparticles,  $\text{TiO}_2\text{-SnS}_2\text{-0.05}$ ,  $\text{TiO}_2\text{-SnS}_2\text{-0.1}$ , and  $\text{TiO}_2\text{-SnS}_2\text{-0.15}$  are 8.37 ns, 10.82 ns, 10.91 ns, 12.44 ns, and 14.39 ns, respectively. The observed trend in lifetime follows the order:  $\text{TiO}_2\text{-SnS}_2\text{-0.15} > \text{TiO}_2\text{-SnS}_2\text{-0.1} > \text{TiO}_2\text{-SnS}_2\text{-0.05} > \text{SnS}_2 > \text{TiO}_2$ .  $\text{TiO}_2\text{-SnS}_2\text{-0.15}$  exhibits a higher average PL decay lifetime indicating a slower recombination rate of photogenerated excitons, indicating more effective charge separation and better photocatalytic efficiency towards the degradation of crystal violet.

### 3.17 Detection of hydroxyl radicals

To prove the formation of hydroxyl radicals during the photodegradation of CV by  $\text{TiO}_2\text{-SnS}_2\text{-0.15}$ , PL spectral studies were performed using terephthalic acid. Terephthalic acid is non-fluorescent but on reaction with hydroxyl radicals, it produces 2-hydroxy terephthalic acid, which is fluorescent.<sup>139</sup> About 40 mg of catalyst ( $\text{TiO}_2\text{-SnS}_2\text{-0.15}$ ) was taken in a beaker containing an aqueous solution of terephthalic acid ( $5 \times 10^{-4}$  M) and NaOH ( $2 \times 10^{-3}$  M). After sunlight irradiation, PL spectra were recorded at periodic time intervals for the supernatant solutions obtained after centrifugation ( $\lambda_{\text{exc}} = 315$  nm). An emission band at 425 nm (Fig. S22) is observed with an increase



in PL intensity as a function of time indicating the generation of hydroxyl radicals with time.

### 3.18 Recyclability and scalability

Photodegradation experiments were performed repeatedly to understand the stability and reusability of  $\text{TiO}_2@\text{SnS}_2$  core-shell nanocomposites. In this experiment, an aqueous solution containing 70 mg of catalyst ( $\text{TiO}_2-\text{SnS}_2-0.15$ ) and 70 mL of CV aqueous solution ( $2 \times 10^{-5}$  M) was kept in the dark (for 30 min) followed by irradiation with sunlight for 60 min. The UV-Vis absorbance spectrum was measured for the supernatant solution obtained after centrifugation. The catalyst was recovered by centrifugation and washed with methanol several times and finally dried in an oven at 60 °C for 12 h. Five cycles of photocatalytic degradation experiments were carried out using the catalyst recovered after each cycle. The recyclability test results (Fig. S23) show a decrease of about 12.5% in photodegradation efficiency of  $\text{TiO}_2-\text{SnS}_2-0.15$  after 5 cycles indicating that  $\text{TiO}_2-\text{SnS}_2-0.15$  is a photocatalyst with good recyclability. Furthermore, to determine the stability of the catalyst ( $\text{TiO}_2-\text{SnS}_2-0.15$ ), characterization of the recovered catalyst was performed. Fig. S24 provides the XRD pattern, FT-IR spectrum and FESEM image of the catalyst recovered after the recyclability test. The post-recyclability EDX analysis results are provided in Table S9. The results indicate no change in the phase or morphology of the catalyst after repeated use indicating its high stability.

Nanomaterials have been explored as catalysts for photodegradation of toxic dyes by easy design using different synthetic approaches. Their size, chemical composition and morphology can be easily controlled using optimized synthetic conditions but due to various environmental concerns and economic viability, their large-scale use for environmental remediation is still limited. In the current work,  $\text{TiO}_2@\text{SnS}_2$  core-shell nanocomposites demonstrate promising photocatalytic activity under laboratory conditions. The synthetic method and photodegradation results in the current study are reproducible, but large-scale production and long-term stability are unexplored.<sup>140</sup>

### 3.19 Potential application of $\text{TiO}_2@\text{SnS}_2$ core-shell nanocomposites as C-2 catalysts

Chemical reactions in which two carbon containing products (e.g., ethanol, ethylene or acetic acid) are formed through C-C coupling reactions are called C-2 reactions. This is particularly relevant for electrocatalytic and photocatalytic  $\text{CO}_2$  reduction and syngas conversion. For a material to be used as a catalyst in a C-2 reaction, the following properties are important: (a) the presence of active sites that can stabilise key intermediates such as  $^*\text{CO}$ ,  $^*\text{CH}_2$  and  $^*\text{CHO}$ , (b) efficient separation of charge carriers (in photocatalysis), and (c) a favourable and stable surface that can promote C-C coupling under the reaction conditions.

Metal sulfide nanoparticles and their nanocomposites have been employed as catalysts for C-2 reactions. For example,  $\text{ZnIn}_2\text{S}_4$  nanosheets activated by nitrogen-doped carbon have been used for electrocatalytic  $\text{CO}_2$  reduction to ethanol.<sup>141</sup>  $\text{SnO}_2/$

$\text{SnS}_2/\text{Cu}_2\text{SnS}_3$  heterojunction has been used for photocatalytic reduction of  $\text{CO}_2$  to ethanol.<sup>142</sup> The  $\text{TiO}_2@\text{SnS}_2$  core-shell nanocomposites are potential materials as catalysts for C-2 reactions. They can catalyze C-C coupling reactions in the following ways. The formation of  $\text{TiO}_2@\text{SnS}_2$  core-shell nanocomposites builds a type-II heterojunction between  $\text{TiO}_2$  and  $\text{SnS}_2$ . On solar irradiation,  $\text{SnS}_2$  absorbs photons and generates an electron-hole pair (see Section 3.14), reducing the recombination of photogenerated excitons and promoting long-lived charge carriers for surface reactions. In the second step, the photogenerated electrons in the CB of  $\text{TiO}_2$  can be used for the formation of intermediate species such as  $^*\text{CO}$ ,  $^*\text{CHO}$  or  $^*\text{CH}_3$  from  $\text{CO}_2/\text{CO}$ .  $\text{SnS}_2$  is well known to stabilize intermediates such as  $^*\text{CO}$ . Furthermore, the C-C coupling can occur in the third step *via* reductive dimerization of surface-bound  $^*\text{CO}$  or  $^*\text{CH}_3$  on the catalyst's surface. This leads to the formation of C-2 species such as acetaldehyde. In the final step, the photogenerated electrons and protons (typically from water oxidation) can hydrogenate acetaldehyde to produce ethanol.

From XPS results (Section 3.8), it was found that charge transfer takes place from core  $\text{TiO}_2$  to shell  $\text{SnS}_2$ , indicating interfacial charge redistribution.<sup>46</sup> An increase in binding energy is observed for Ti 2p and O 1s, whereas a decrease in binding energy is observed for Sn 3d and S 2p in the  $\text{TiO}_2@\text{SnS}_2$  core-shell nanocomposites. This suggests that there is more electron density on the surface of  $\text{SnS}_2$  after the formation of  $\text{TiO}_2@\text{SnS}_2$  core-shell nanocomposites. The electron-rich  $\text{SnS}_2$  surface is beneficial in stabilizing electrophilic species (C-1) such as CHO and provides them sufficient residence time for C-C coupling reactions and can enhance catalytic activity compared to the individual components.

## 4 Conclusions

In the present study,  $\text{TiO}_2@\text{SnS}_2$  core-shell nanocomposites were synthesized using the thermal decomposition method using different  $[\text{Sn}^{4+}]:[\text{S}^{2-}]$  ratios. The core-shell nanocomposites were characterized using several analytical techniques. The XRD results confirmed the presence of both  $\text{TiO}_2$  and  $\text{SnS}_2$  phases in the core-shell nanocomposites. FESEM and TEM analyses confirmed uniform coating of  $\text{SnS}_2$  nanoparticles on the  $\text{TiO}_2$  microspheres indicating their core-shell structure. The  $\text{TiO}_2@\text{SnS}_2$  core-shell nanocomposites demonstrate good catalytic activity towards the photodegradation of CV in aqueous solutions under sunlight. The photocatalytic efficiency of  $\text{TiO}_2@\text{SnS}_2$  core-shell nanocomposites is better than that of the individual constituents and other metal-sulfide based nanocomposites that are reported in the literature. The  $\text{TiO}_2@\text{SnS}_2$  core-shell nanocomposites, reported in the present study, have other potential applications, e.g., sodium-ion batteries, gas sensors, water splitting, *etc.*

## Author contributions

Nainy Khera: Methodology, data collection and interpretation, writing – original draft. Pethaiyan Jeevanandam: Conceptualization, project administration



## Conflicts of interest

There are no conflicts to declare.

## Data availability

All the data supporting this study have been included in the main manuscript and the SI.

Some additional data supporting this article have been included as part of SI. See DOI: <https://doi.org/10.1039/d5na00533g>.

## Acknowledgements

Nainy Khera acknowledges Council of Scientific and Industrial Research (CSIR), Govt of India for the award of a fellowship (JRF/SRF). The authors express gratitude to Institute Instrumentation Centre (IIT Roorkee) for helping with necessary instrumental facilities. Thanks are due to the Department of Metallurgical and Materials Engineering, IIT Roorkee for providing the HRTEM facility.

## References

- 1 Z. Kılıç, *Int. J. Hydrol.*, 2020, **4**, 239–241.
- 2 A. Rafiq, M. Ikram, S. Ali, F. Niaz, M. Khan, Q. Khan and M. Maqbool, *J. Ind. Eng. Chem.*, 2021, **97**, 111–128.
- 3 R. Al-Tohamy, S. S. Ali, F. Li, K. M. Okasha, Y. A. G. Mahmoud, T. Elsamahy, H. Jiao, Y. Fu and J. Sun, *Ecotoxicol. Environ. Saf.*, 2022, **231**, 113160.
- 4 Z. Zheng, J. He, Z. Zhang, A. Kumar, M. Khan, C. W. Lung and I. M. C. Lo, *Environ. Sci. Nano*, 2024, **11**, 1784–1816.
- 5 C. C. Chen, C. S. Lu, Y. C. Chung and J. L. Jan, *J. Hazard. Mater.*, 2007, **141**, 520–528.
- 6 Y. Zhang, X. Yu, H. Liu, X. Lian, B. Shang, Y. Zhan, T. Fan, Z. Chen and X. Yi, *Environ. Sci. Nano*, 2021, **8**, 2049–2058.
- 7 Y. Zhang, Z. Zhang, Y. Zhang, Y. Li and Y. Yuan, *J. Colloid Interface Sci.*, 2023, **651**, 117–127.
- 8 X. Yin, L. Liu and F. Ai, *Front. Chem.*, 2021, **9**, 1–9.
- 9 Y. Wan, J. Chen, J. Zhan and Y. Ma, *J. Environ. Chem. Eng.*, 2018, **6**, 6079–6087.
- 10 W. Xu, S. Zhu, Y. Liang, Z. Li, Z. Cui, X. Yang and A. Inoue, *Sci. Rep.*, 2015, **5**, 18125.
- 11 B. Sheng, J. Liu, Z. Li, M. Wang, K. Zhu, J. Qiu and J. Wang, *Mater. Lett.*, 2015, **144**, 153–156.
- 12 M. Baláž, E. Dutková, Z. Bujnáková, E. Tóthová, N. G. Kostova, Y. Karakirova, J. Briančin and M. Kaňuchová, *J. Alloys Compd.*, 2018, **746**, 576–582.
- 13 R. R. Srivastava, P. Kumar Vishwakarma, U. Yadav, S. Rai, S. Umrao, R. Giri, P. S. Saxena and A. Srivastava, *Front. Nanotechnol.*, 2021, **3**, 1–13.
- 14 D. Hong, W. Zang, X. Guo, Y. Fu, H. He, J. Sun, L. Xing, B. Liu and X. Xue, *ACS Appl. Mater. Interfaces*, 2016, **8**, 21302–21314.
- 15 A. Sadollahkhani, O. Nur, M. Willander, I. Kazeminezhad, V. Khranovskyy, M. O. Eriksson, R. Yakimova and P. O. Holtz, *Ceram. Int.*, 2015, **41**, 7174–7184.
- 16 H. D. Abdul kader, I. Sh. Mohammed and S. H. Ammar, *Environ. Nanotechnol. Monit. Manag.*, 2022, **17**, 100664.
- 17 J. Chen, Y. Liao, X. Wan, S. Tie, B. Zhang, S. Lan and X. Gao, *J. Solid State Chem.*, 2020, **291**, 121652.
- 18 X. Dong, J. Deng, M. Ge, S. Lu and Q. Zhu, *Chem. Phys. Lett.*, 2023, **833**, 140950.
- 19 M. F. Mubarak, H. Selim and R. Elshypany, *J. Environ. Health Sci. Eng.*, 2022, **20**, 265–280.
- 20 A. Habtamu and M. Ujihara, *RSC Adv.*, 2023, **13**, 12926–12940.
- 21 Q. Gao, J. Li, B. Liu and C. Liu, *J. Alloys Compd.*, 2023, **931**, 167430.
- 22 T. T. Salunkhe, V. Kumar, A. N. Kadam, M. Mali and M. Misra, *Ceram. Int.*, 2024, **50**, 1826–1835.
- 23 X. Zhang, X. Jia, R. Xu, X. Lu, H. Liu and Y. Niu, *J. Alloys Compd.*, 2022, **923**, 166315.
- 24 V. Gadore, S. R. Mishra and M. Ahmaruzzaman, *J. Hazard. Mater.*, 2023, **444**, 130301.
- 25 V. Gadore, S. R. Mishra and M. Ahmaruzzaman, *J. Environ. Manage.*, 2023, **334**, 117496.
- 26 G. Kumar, *J. Inorg. Organomet. Polym. Mater.*, 2023, **33**, 2710–2720.
- 27 J. Srivind, V. S. Nagarethinam, M. Suganya, S. Balamurugan, D. Prabha and A. R. Balu, *Mater. Sci. Eng. B*, 2020, **255**, 114530.
- 28 Q. Li, S. He, L. Wang, J. Song, J. Wang, C. Shao, Z. Tian and Y. Liu, *CrystEngComm*, 2023, **25**, 2882–2891.
- 29 V. Gadore, S. R. Mishra and M. Ahmaruzzaman, *Chemosphere*, 2024, **359**, 142343.
- 30 Y. Zhang, L. Hu, H. Zhou, H. Wang and Y. Zhang, *ACS Appl. Nano Mater.*, 2022, **5**, 391–400.
- 31 G. Gautam, M. Kumar and B. Singh, *Mater. Today Proc.*, 2022, **62**, 3239–3243.
- 32 H. Wei, Y. Zhang, Y. Zhang and Y. Zhang, *Colloids Interface Sci. Commun.*, 2021, **45**, 100550.
- 33 P. Salimi Kuchi, H. Roshan and M. H. Sheikhi, *J. Alloys Compd.*, 2020, **816**, 152666.
- 34 X. Meng, M. Bi, Q. Xiao and W. Gao, *Sens. Actuators, B*, 2022, **359**, 131612.
- 35 D. Gu, W. Liu, J. Wang, J. Yu, J. Zhang, B. Huang, M. N. Rumyantseva and X. Li, *Chemosensors*, 2022, **10**, 165.
- 36 J. Yan, Q. Li, Y. Hao, C. Dai and Y. Chen, *Funct. Mater. Lett.*, 2020, **13**, 1–4.
- 37 A. K. Dwivedi and S. Tripathi, *IEEE Trans. Electron Devices*, 2023, **70**, 2378–2383.
- 38 L. Li, Z. Wei, S. Huang, C. Li, Q. Lu and J. Ma, *J. Mater. Sci. Mater. Electron.*, 2022, **33**, 18884–18896.
- 39 W. Zhao, Z. Wei, X. Zhang, M. Ding and S. Huang, *Mater. Res. Bull.*, 2020, **124**, 110749.
- 40 T. Luttrell, S. Halpegamage, J. Tao, A. Kramer, E. Sutter and M. Batzill, *Sci. Rep.*, 2015, **4**, 4043.
- 41 C. S. Diko, M. Abitonze, Y. Liu, Y. Zhu and Y. Yang, *Nanomaterials*, 2022, **12**, 4497.
- 42 X. Guo, F. Zhang, Y. Zhang and J. Hu, *J. Mater. Chem. A*, 2023, **11**, 7331–7343.
- 43 L. A. Burton, T. J. Whittles, D. Hesp, W. M. Linhart, J. M. Skelton, B. Hou, R. F. Webster, G. O'Dowd, C. Reece,



D. Cherns, D. J. Fermin, T. D. Veal, V. R. Dhanak and A. Walsh, *J. Mater. Chem. A*, 2016, **4**, 1312–1318.

44 S. Mondal, S. Das and U. K. Gautam, *J. Colloid Interface Sci.*, 2021, **603**, 110–119.

45 L. Deng, H. Liu, X. Gao, X. Su and Z. Zhu, *Ceram. Int.*, 2016, **42**, 3808–3815.

46 N. Carl, M. Fiaz, H. S. Oh and Y. K. Kim, *Catalysts*, 2024, **14**, 442.

47 J. Zheng, H. Yang, F. Zheng, F. Liu, L. Lin and S. Li, *J. Phys. Chem. C*, 2022, **126**, 11629–11635.

48 J. Gao, X. Sun, L. Zheng, G. He, Y. Wang, Y. Li, Y. Liu, J. Deng, M. Liu and J. Hu, *New J. Chem.*, 2021, **45**, 16131–16142.

49 S. Ding, W. Gan, J. Guo, R. Chen, R. Liu, Z. Zhao, J. Li, M. Zhang and Z. Sun, *J. Mater. Chem. C*, 2024, **12**, 7079–7094.

50 P. Bharathi, S. Harish, M. Shimomura, M. K. Mohan, J. Archana and M. Navaneethan, *Chemosphere*, 2024, **346**, 140486.

51 Q. Sun, Y. Li, J. Hao, S. Zheng, T. Zhang, T. Wang, R. Wu, H. Fang and Y. Wang, *ACS Appl. Mater. Interfaces*, 2021, **13**, 54152–54161.

52 W. Yu, D. Chen, J. Li and Z. Zhang, *Crystals*, 2023, **13**, 1–11.

53 J. Zhang, H. Shen, Y. Li, X. Li, J. Sun, D. Yan, X. Jin and X. Wu, *Surf. Interfaces*, 2024, **54**, 105136.

54 J. Shao, X.-T. Wang, H. Xu, X.-D. Zhao, J.-M. Niu, Z.-D. Zhang, Y.-L. Huang and J.-Z. Duan, *J. Electrochem. Soc.*, 2021, **168**, 016511.

55 H. Yao and L. Liu, *Vacuum*, 2024, **222**, 113030.

56 S. Zhu, G. Wu, Z. Liu, S. Zhao, D. Cao, C. Li and G. Liu, *Ceram. Int.*, 2023, **49**, 5893–5904.

57 S. Shanmugaratnam, B. Selvaratnam, A. Baride, R. Koodali, P. Ravirajan, D. Velauthapillai and Y. Shivatharsiny, *Catalysts*, 2021, **11**, 589.

58 P. Yao, S. Yu, H. Shen, J. Yang, L. Min, Z. Yang and X. Zhu, *New J. Chem.*, 2019, **43**, 16748–16752.

59 L. Sun, Z. Zhao, S. Li, Y. Su, L. Huang, N. Shao, F. Liu, Y. Bu, H. Zhang and Z. Zhang, *ACS Appl. Nano Mater.*, 2019, **2**, 2144–2151.

60 Y. Wu, G. Lin, X. Zhou, J. Chen, J. Zhuang, Q. Chen, Y. Luo, D. Lu, V. Ganesh and R. Zeng, *J. Electroanal. Chem.*, 2020, **857**, 113740.

61 M. Kovacic, H. Kusic, M. Fanetti, U. L. Stangar, M. Valant, D. D. Dionysiou and A. L. Bozic, *Environ. Sci. Pollut. Res. Int.*, 2017, **24**, 19965–19979.

62 L. Truong-Phuoc, K. C. Christoforidis, F. Vigneron, V. Papaefthimiou, G. Decher, N. Keller and V. Keller, *ACS Appl. Mater. Interfaces*, 2016, **8**, 34438–34445.

63 J. Lin, Y. Liu, Y. Liu, C. Huang, W. Liu, X. Mi, D. Fan, F. Fan, H. Lu and X. Chen, *ChemSusChem*, 2019, **12**, 961–967.

64 K. C. Christoforidis, A. Sengele, V. Keller and N. Keller, *ACS Appl. Mater. Interfaces*, 2015, **7**, 19324–19334.

65 M. Li, H. Liu, T. Lv and M. Ding, *J. Mater. Chem. A*, 2018, **6**, 3488–3499.

66 H. She, H. Zhou, L. Li, Z. Zhao, M. Jiang, J. Huang, L. Wang and Q. Wang, *ACS Sustain. Chem. Eng.*, 2019, **7**, 650–659.

67 J. Wang, X. Li, J. Zhu, H. Li and X. Le, *Nanoscale*, 2013, **5**, 1876–1881.

68 S. Tanaka, D. Nogami, N. Tsuda and Y. Miyake, *J. Colloid Interface Sci.*, 2009, **334**, 188–194.

69 C. Rosiles-Perez, M. Ocampo Gaspar, O. J. Padilla González, L. F. Román Flores and A. E. Jiménez- González, *Emergent Mater.*, 2024, **7**, 1445–1462.

70 P. Somasundaran, B. Markovic, X. Yu and S. Krishnakumar, *Handb. Surf. Colloid Chem. Second Ed.*, CRC Press, Taylor and Francis Group, London, New York, 2002, pp. 387–436.

71 P. Rana and P. Jeevanandam, *ChemNanoMat*, 2024, **10**, 1–11.

72 Profile Solar, Solar PV analysis of Roorkee, India, <https://profilesolar.com/locations/India/Roorkee> accessed July 11, 2025.

73 A. H. Ragab, N. F. Gumaah, A. A. El Aziz Elfiky and M. F. Mubarak, *BMC Chem.*, 2024, **18**, 121.

74 L. B. Chandrasekar, R. Chandramohan, R. Vijayalakshmi and S. Chandrasekaran, *Int. Nano Lett.*, 2015, **5**, 71–75.

75 J. Madhavi, *SN Appl. Sci.*, 2019, **1**, 1–12.

76 A. Dastider, H. Saha, M. J. F. Anik, M. Jamal and M. M. Billah, *RSC Adv.*, 2024, **14**, 11677–11693.

77 M. S. Jamal, S. A. Shahahmadi, P. Chelvanathan, H. F. Alharbi, M. R. Karim, M. Ahmad Dar, M. Luqman, N. H. Alharthi, Y. S. Al-Harthi, M. Aminuzzaman, N. Asim, K. Sopian, S. K. Tiong, N. Amin and M. Akhtaruzzaman, *Results Phys.*, 2019, **14**, 102360.

78 S. Wadhai and P. Thakur, *Environ. Sci. Pollut. Res. Int.*, 2024, **31**, 60836–60851.

79 P. Praveen, G. Viruthagiri, S. Mugundan and N. Shanmugam, *Spectrochim. Acta A Mol. Biomol. Spectrosc.*, 2014, **117**, 622–629.

80 H. Liu, C. Du, H. Bai, Y. Su, D. Wei, Y. Wang, G. Liu and L. Yang, *J. Mater. Sci.*, 2018, **53**, 10743–10757.

81 Z. Wu, Y. Xue, Y. Zhang, J. Li and T. Chen, *RSC Adv.*, 2015, **5**, 24640–24648.

82 R. Gaur and P. Jeevanandam, *J. Nanosci. Nanotechnol.*, 2017, **18**, 165–177.

83 A. K. El-Sawaf, A. A. Nassar, A. A. El Aziz Elfiky and M. F. Mubarak, *Polym. Bull.*, 2024, **81**, 12451–12476.

84 S. Balu, K. Uma, G. T. Pan, T. C. K. Yang and S. K. Ramaraj, *Materials*, 2018, **11**, 1030.

85 Y. L. Pang, S. Lim and R. K. L. Lee, *Environ. Sci. Pollut. Res. Int.*, 2020, **27**, 34638–34652.

86 M. Sathish, S. Mitani, T. Tomai, A. Unemoto and I. Honma, *J. Solid State Electrochem.*, 2012, **16**, 1767–1774.

87 B. Liu, W. Wang, H. Li, Z. Jian, Y. Xing and S. Zhang, *Int. J. Electrochem. Sci.*, 2018, **13**, 6870–6879.

88 M. F. Mubarak, H. Selim, H. B. Hawash and M. Hemdan, *Environ. Sci. Pollut. Res. Int.*, 2024, **31**, 2297–2313.

89 S. Landi, I. R. Segundo, E. Freitas, M. Vasilevskiy, J. Carneiro and C. J. Tavares, *Solid State Commun.*, 2022, **341**, 1–7.

90 P. R. Jubu, E. Danladi, U. I. Ndeze, O. Adedokun, S. Landi, A. J. Haider, A. T. Adepoju, Y. Yusof, O. S. Obaseki and F. K. Yam, *Results Opt.*, 2024, **14**, 100606.



91 A. Saha, A. Moya, A. Kahnt, D. Iglesias, S. Marchesan, R. Wannemacher, M. Prato, J. J. Vilatela and D. M. Guldi, *Nanoscale*, 2017, **9**, 7911–7921.

92 C. C. Mercado, F. J. Knorr, J. L. McHale, S. M. Usmani, A. S. Ichimura and L. V. Saraf, *J. Phys. Chem. C*, 2012, **116**, 10796–10804.

93 F. J. Knorr, D. Zhang and J. L. McHale, *Langmuir*, 2007, **23**, 8686–8690.

94 D. Prabha, S. Ilangovan, J. Srivind, M. Suganya, S. Anitha, S. Balamurugan and A. R. Balu, *J. Mater. Sci. Mater. Electron.*, 2017, **28**, 15556–15564.

95 I. Iatsunskyi, M. Kempinski, G. Nowaczyk, M. Jancelewicz, M. Pavlenko, K. Zalesski and S. Jurga, *Appl. Surf. Sci.*, 2015, **347**, 777–783.

96 A. K. Mohamedkhair, Q. A. Drmosh and Z. H. Yamani, *Front. Mater.*, 2019, **6**, 1–10.

97 S. Yan, K. Li, Z. Lin, H. Song, T. Jiang, J. Wu and Y. Shi, *RSC Adv.*, 2016, **6**, 32414–32421.

98 P. van der Heide, *X-Ray Photoelectron Spectroscopy: an Introduction to Principles and Practices*, John Wiley & Sons, Inc., Hoboken, New Jersey, 2011.

99 S. Jain, N. Kumar, S. Sharma, D. Parmar, R. K. Sharma, M. Tahir, K. Kumari and G. Rani, *Mater. Today Sustain.*, 2023, **24**, 100539.

100 M. Andrulevičius, S. Tamulevičius, Y. Gnatyuk, N. Vityuk, N. Smirnova and A. Eremenko, *Mater. Sci.*, 2008, **14**, 8–14.

101 L. Shi, C. Xu, X. Sun, H. Zhang, Z. Liu, X. Qu and F. Du, *J. Mater. Sci.*, 2018, **53**, 11329–11342.

102 D. M. Mwangangi, T. A. Makhetha, J. C. Ngila and L. N. Dlamini, *FlatChem*, 2025, **51**, 100865.

103 S. Ahmed, M. Ahmad, M. H. Yousaf, S. Haider, Z. Imran, S. S. Batool, I. Ahmad, M. I. Shahzad and M. Azeem, *Front. Chem.*, 2022, **10**, 1–9.

104 A. Balakrishnan, J. D. Groeneveld, S. Pokhrel and L. Mädler, *Chem.-Eur. J.*, 2021, **27**, 6390–6406.

105 J. Gajendiran and V. Rajendran, *Adv. Nat. Sci. Nanosci. Nanotechnol.*, 2011, **2**, 015001.

106 H. Zhang, T. Van Pelt, A. N. Mehta, H. Bender, I. Radu, M. Caymax, W. Vandervorst and A. Delabie, *2D Mater.*, 2018, **5**, 035006.

107 S. Samira and A. Raja P, *J. Thermodyn. Catal.*, 2012, **3**, 1–6.

108 R. K. Upadhyay, M. Sharma, D. K. Singh, S. S. Amritphale and N. Chandra, *Sep. Purif. Technol.*, 2012, **88**, 39–45.

109 G. Xing, L. Zhang, Y. Zhao, S. Li, T. Li, T. Lv, C. Yu and C. Zhao, *J. Mol. Struct.*, 2023, **1274**, 134409.

110 F. Karimi, H. R. Rajabi and L. Kavoshi, *Ultrason. Sonochem.*, 2019, **57**, 139–146.

111 S. D. Oladipo and B. Omondi, *J. Coord. Chem.*, 2022, **75**, 2170–2188.

112 M. Sharma, T. Jain, S. Singh and O. P. Pandey, *Sol. Energy*, 2012, **86**, 626–633.

113 Z. A. Piranshahi, M. Behbahani and F. Zeraatpisheh, *Appl. Organomet. Chem.*, 2018, **32**, 1–11.

114 A. Dasari and V. Guttena, *Mater. Today Commun.*, 2019, **19**, 157–169.

115 V. Manikandan, R. Elancheran, P. Revathi, P. Suganya and K. Krishnasamy, *Bull. Mater. Sci.*, 2020, **43**, 265.

116 A. K. Garg, B. Singh, S. Naskar, R. K. Prajapati, C. Dalal and S. K. Sonkar, *Langmuir*, 2023, **39**, 11036–11047.

117 A. Nezamzadeh-Ejhieh and Z. Banan, *Desalination*, 2012, **284**, 157–166.

118 V. Balchander, D. Ayodhya and R. S. Sunder, *Inorg. Chem. Commun.*, 2024, **162**, 112181.

119 R. Mohammed and M. E. M. Ali, *Environ. Nanotechnol., Monit. Manag.*, 2023, **20**, 100885.

120 G. Murugadoss, S. Salla, M. R. Kumar, N. Kandhasamy, H. Al Garalleh, M. Garaleh, K. Brindhadevi and A. Pugazhendhi, *Environ. Res.*, 2023, **220**, 115171.

121 H. Xie, T. Zeng, S. Jin, Y. Li, X. Wang, X. Sui and X. Zhao, *J. Nanosci. Nanotechnol.*, 2013, **13**, 1461–1466.

122 S. V. P. Vattikuti, I. L. Ngo and C. Byon, *Solid State Sci.*, 2016, **61**, 121–130.

123 B. S. Goud, G. Kooyada, J. H. Jung, G. R. Reddy, J. Shim, N. D. Nam and S. V. P. Vattikuti, *Int. J. Hydrogen Energy*, 2020, **45**, 18961–18975.

124 H. Fakhri, A. R. Mahjoub and A. H. C. Khavar, *Appl. Surf. Sci.*, 2014, **318**, 65–73.

125 C. Yu, K. Wang, P. Yang, S. Yang, C. Lu, Y. Song, S. Dong, J. Sun and J. Sun, *Appl. Surf. Sci.*, 2017, **420**, 233–242.

126 G. Murugadoss, S. Muruganandam, M. R. Kumar and A. Pugazhendhi, *Chemosphere*, 2023, **336**, 139100.

127 Y. Dan, J. Xu, J. Jian, L. Meng, P. Deng, J. Yan, Z. Yuan, Y. Zhang and H. Zhou, *Molecules*, 2023, **28**, 6882.

128 Q. Wei, Q. Dong, D. W. Sun and H. Pu, *Spectrochim. Acta - Part A Mol. Biomol. Spectrosc.*, 2023, **285**, 121895.

129 V. N. Nguyen, D. T. Tran, M. T. Nguyen, T. T. T. Le, M. N. Ha, M. V. Nguyen and T. D. Pham, *Res. Chem. Intermed.*, 2018, **44**, 3081–3095.

130 N. P. de Moraes, F. N. Silva, M. L. C. P. da Silva, T. M. B. Campos, G. P. Thim and L. A. Rodrigues, *Mater. Chem. Phys.*, 2018, **214**, 95–106.

131 P. Ghasemipour, M. Fattah, B. Rasekh and F. Yazdian, *Sci. Rep.*, 2020, **10**, 4414.

132 H. J. Fan, S. T. Huang, W. H. Chung, J. L. Jan, W. Y. Lin and C. C. Chen, *J. Hazard. Mater.*, 2009, **171**, 1032–1044.

133 A. Farajollahi, A. Poursattar Marjani, N. Noroozi Pesyan and H. Alamgholiloo, *Appl. Surf. Sci.*, 2023, **622**, 156903.

134 M. Bledowski, L. Wang, A. Ramakrishnan, O. V. Khavryuchenko, V. D. Khavryuchenko, P. C. Ricci, J. Strunk, T. Cremer, C. Kolbeck and R. Beranek, *Phys. Chem. Chem. Phys.*, 2011, **13**, 21511–21519.

135 O. P. Kumar, M. N. Ashiq, M. Ahmad, S. Anjum and A. ur Rehman, *J. Mater. Sci. Mater. Electron.*, 2020, **31**, 21082–21096.

136 Q. U. Ain, U. Rasheed, M. Yaseen, H. Zhang and Z. Tong, *J. Hazard. Mater.*, 2020, **397**, 122758.

137 Z. Cao, Y. Yin, P. Fu, D. Li, Y. Zhou, Y. Deng, Y. Peng, W. Wang, W. Zhou and D. Tang, *Nanoscale Res. Lett.*, 2019, **14**, 1–9.

138 H. Wang, L. Xu, R. Zhang, Z. Ge, W. Zhang, J. Xu, Z. Ma and K. Chen, *Nanoscale Res. Lett.*, 2015, **10**, 128.

139 G. Žerjav, A. Albreht, I. Vovk and A. Pintar, *Appl. Catal. A Gen.*, 2020, **598**, 117566.



140 K. R. M. Oraby, A. Villalonga, F. S. M. Hassan, M. A. Zayed, M. F. Mubarak, I. Ojeda, A. Sánchez and R. Villalonga, *Process Biochem.*, 2025, **148**, 10–16.

141 F. Cai, X. Hu, F. Gou, Y. Chen, Y. Xu, C. Qi and D. K. Ma, *Appl. Surf. Sci.*, 2023, **611**, 155696.

142 F. Wang, S. Zhang, W. Jing, H. Qiu, Y. Liu and L. Guo, *J. Mater. Sci. Technol.*, 2024, **189**, 146–154.

